POLITECNICO
MILANO 1863

SCUOLA DI INGEGNERIA INDUSTRIALE
E DELL'INFORMAZIONE

Prandtl Effects in AM Cooling Channels

Tesi di Laurea Magistrale in
Energy Engineering - Ingegneria Energetica

Gabriele Moser, 10682626

Advisor:
Prof. Andrea Lucchini

Co-advisors:
Dr. Mats Kinell

Academic year:
2024-2025

Abstract: This thesis focuses on the study of cooling channels manufactured by Additive Manufacturing (AM). This technology provides a high degree of design freedom, enabling new optimization possibilities for heat exchangers and turbomachinery components. However, the anisotropic surface roughness typical of the AM printing process strongly influences flow dynamics and thermal performance, making the development of specific predictive correlations necessary.
The aim of this work is to experimentally investigate the influence of the Prandtl number on heat transfer, with water as the cooling fluid, in cylindrical channels manufactured using the most widely adopted additive manufacturing technique for metals, Laser Powder Bed Fusion (LPBF). Tests were conducted on a smooth reference channel, for validation purposes, and on two additively manufactured test objects with different hydraulic diameters.
The results confirm that the experimental rig can reproduce classical correlations for the turbulent regime, both for pressure drop and heat transfer, for the smooth test object. Analyses on the AM-printed cooling channels show that an increase in the Prandtl number does not always lead to an increase in heat transfer, in contrast with classical theory. To capture this effect, a new correlation is proposed based on the experimental data of the two tested cooling channels. This work therefore represents a first step in the prediction and understanding of this new phenomenon, and further investigations are necessary.

Key-words: heat transfer; additive manufacturing; prandtl number; surface roughness; cooling channels

1. Introduction

1.1. Siemens Energy AB

Siemens Energy AB is a key subsidiary of Siemens Energy in Sweden, a global leader in the energy sector committed to driving the transition toward a sustainable future. Operating in over 90 countries, Siemens Energy focuses on delivering innovative solutions for energy generation, transmission and utilization, while actively reducing carbon emissions [16]. The main center of Siemens Energy AB is located in Finspång, where the development and production of industrial gas turbines and compressors take place. With over 100 years of experience, the Finspång site has remained at the forefront of innovation, providing integrated solutions in electrification, automation, and digitalization for the manufacturing and process industries [17]. Research and Development ($R\&D$) is a core focus in Finspång´s factory. One of the current goals is to integrate the Additive

Manufacturing (AM) printing process into gas turbine production [18]. In the Fluid Dynamics Lab, where this thesis was conducted under the guidance of Dr. Mats Kinell, tests are performed to evaluate the impact of Additive Manufacturing induced roughness on flow dynamics and heat transfer.

1.2. Additive Manufacturing

"Additive manufacturing is revolutionizing the development and production of components in the energy sector. 3D printing makes it possible to produce almost any structure. It accelerates rapid prototyping, which in turn shortens the design and market introduction of new components and devices." says Hubertus Breuer [3], technology journalist. This technology is investigated to optimize the design and production of critical turbine components, reducing manufacturing complexity and improving performance. For example, it has been used to manufacture burners as single pieces, whereas they previously required numerous individual parts and welds. This reduces error tolerance during production, ensures greater consistency, and minimizes production issues. The design has also been significantly improved [3].
The additive manufacturing technique used to print the channels tested in this work is Laser Powder Bed Fusion (LPBF), in the commercial variant known as Direct Metal Laser Sintering (DMLS), widely used for metal 3D printing [23]. In this process, a high-intensity laser beam, generated by a fiber laser and directed by scanning mirrors through focusing lenses, selectively melts regions of metal powder on the bed, following the cross-sectional geometry of the 3D CAD model. After laser exposure, the build platform is lowered by a depth equal to the desired layer thickness using a piston mechanism, while the powder dispenser piston raises its platform to supply fresh metal powder. The recoater arm then uniformly distributes a new layer of powder on top of the previous one, and the cycle is repeated until the final part is completed [53]. Figure 1 provides a schematic overview of the process.

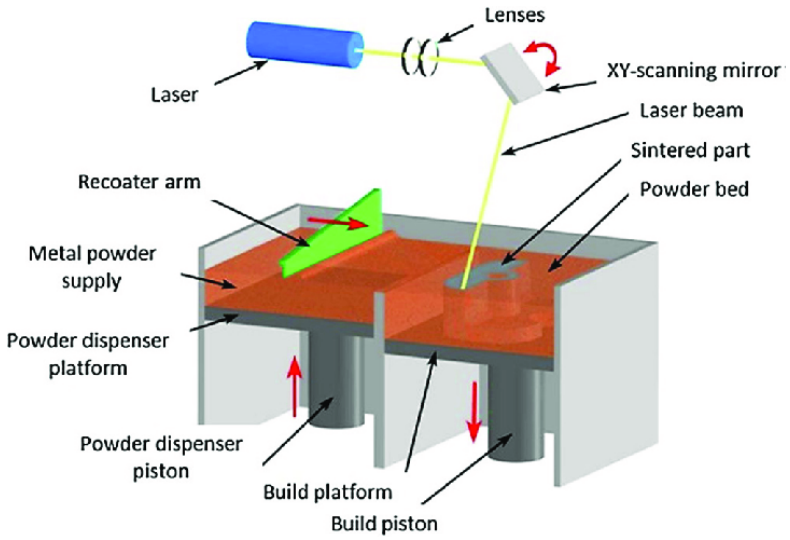

Figure 1: Direct Metal Laser Sintering (DMLS) Setup [13]

This project began with the aim of collecting data for cooling channels, which typically use air, in first-stage turbine blades that may potentially be manufactured using DMLS technique in the future. However, it is not limited to that specific application: the results can also be applied to different types of heat exchangers using various fluids, as the research is still in its early stages.

1.3. Research Scope

The long-term goal of the ongoing research in the laboratory is to establish an empirical correlation that accurately predicts how additive manufacturing–induced surface roughness affects heat transfer. This thesis represents a specific contribution to that broader objective by investigating the influence of the Prandtl number on heat transfer through experiments conducted with water in DMLS printed channels. Other experimental rigs in the laboratory address complementary aspects of the problem, including air-flow tests in the same channels, as well as two local experimental rigs: one equipped with Particle Image Velocimetry (PIV) technology to assess the local influence of the roughness on the flow field, and another using a high-resolution infrared camera to capture the local effects on heat transfer. This work builds upon the efforts of previous students. The

experimental rig is still evolving, as demonstrated by the modifications implemented during this project, and further improvements are expected in the future.

1.4. My Contribution

A new hydraulic circuit was designed and built to enhance control over both the mass flow rate and the water temperature, while also improving water quality through the addition of a filter. These modifications significantly increased the overall stability of the system and made the testing procedure faster and more straightforward. As a result, the rig was able to better reproduce well-established correlations for both pressure drop and heat transfer during validation tests with a machined smooth channel.
Two DMLS printed test objects were tested over a range of Prandtl numbers, with the heat transfer results analyzed in light of the data obtained in the past from the previous version of the rig, allowing for an initial assessment of the influence of this parameter on heat transfer.

1.5. Literature Review

This section begins with an overview of the new design possibilities for heat exchangers enabled by additive manufacturing, then reviews existing studies that investigate how the unique surface roughness induced by AM influences thermal performance and pressure drop in printed channels, including both experimental investigations and CFD analyses.

1.5.1 Innovative AM Design

Additive manufacturing opens a new chapter in the design and development of heat exchangers, enabling topology-optimized geometries, which are not obtainable through conventional methods [37], to maximize thermal performance and minimize pressure drop [48]. It allows the creation of lightweight heat exchangers with enhanced surface areas and monolithic bonds, eliminating the need for welding or brazing and potentially reducing production cycle times [47] [37]. Design freedom in additive manufacturing also facilitates the emergence of artificial intelligence as a powerful tool to optimize the design and production processes of heat exchangers [35].
In the energy sector, AM heat exchangers have been proposed for compact condensers in vapor compression systems [54], as well as for high-pressure and high-temperature applications, such as supercritical CO_2 Brayton cycles and concentrated solar power plants (CSP) [42], utilizing ceramic materials in this case [15] [11], to enhance the global efficiency. Another key application is in electronic heat sinks, where the design flexibility enabled by additive manufacturing allows complex microchannel configurations that are not achievable with traditional manufacturing [9]. Collins *et al.* [9] reported a 40–90% reduction in pressure drop, depending on flow rate, with a DMLS printed manifold microchannel heat sink compared to straight channel designs, due to its complicated geometry. However, the high internal surface roughness promotes the onset of turbulence at lower Reynolds numbers ($Re_{cr} \approx 600 - 800$), compared to smooth channels, a critical factor in microchannel heat sink design where laminar flow is typically assumed. Similarly, Kong *et al.* [32] obtained a pressure drop reduction of 38–70% and a total thermal resistance reduction of 24–44% with a monolithically additively manufactured manifold–microchannel heat sink, compared to a conventional microchannel heat sink. In aerospace applications, beyond the topology optimization benefits already discussed, additive manufacturing may enable weight reduction through the creation of compact heat exchangers. However, several challenges remain for future adoption, including the limited repeatability in producing thin sections, the difficulty of cleaning complex internal channels to remove entrapped powder, and the high internal surface roughness [6]. Comparable considerations apply to the automotive sector, where AM designs reduce the weight and volume of heat exchangers while increasing their surface area, meeting critical design requirements [47].

1.5.2 Experimental Works

The effects of AM-induced surface roughness on pressure drop and heat transfer, identified as a key limitation for printed heat exchangers in the previous section, have been a primary focus of experimental investigations.
Stimpson *et al.* [45] [46] conducted one of the first studies related to the topic. They investigated straight rectangular channels made of CoCr and Inconel 718, testing them in coupon configurations with either 16 or 24 channels. The samples were printed using Direct Metal Laser Sintering (DMLS), with varying cross-sectional dimensions. Air was used as the cooling fluid. For the pressure drop, in the laminar regime, higher relative roughness led to an increase in the friction factor and an earlier onset of the transitional region. These effects deviated from the classical laminar flow theory, consistently with observations reported by Huang *et al.* [28] and Collins *et al.* [9]. In the turbulent regime, a fully rough flow behavior was observed: the friction factor

became independent of the Reynolds number. The equivalent relative roughness (ϵ/D) was obtained by fitting the Colebrook-White equation to the measured friction factor for each coupon. Higher relative roughness mainly resulted from a reduction in the hydraulic diameter, since the absolute roughness depends on the printing process and the alloy used [12] [5]. This explains the higher friction factors observed in channels with smaller hydraulic diameters. For heat transfer, the channels with higher Nusselt numbers also exhibited higher friction factors, all showing a significant enhancement compared to the smooth reference condition. The data aligned well with the simplified correlation for Nusselt number augmentation as a function of friction factor augmentation proposed by Norris [39]:

$$\frac{Nu}{Nu_0} = \left(\frac{f_D}{f_{D0}}\right)^n \tag{1}$$

where $n = 0.68Pr^{0.215}$.
In the subsequent study [46], Stimpson *et al.* derived an empirical correlation from the same experimental dataset, expressing the Nusselt number as a function of Reynolds number, Prandtl number, and friction factor:

$$Nu = \frac{(Re^{0.5} - 29) \cdot Pr \cdot \sqrt{f_D/8}}{0.6 \cdot (1 - Pr^{2/3})} \tag{2}$$

This correlation showed a variation of $\pm 15\%$ when using friction factors estimated experimentally. It should be noted that the correlation was validated only with air as the working fluid ($Pr \approx 0.7$), without any variation of the Prandtl number. Therefore, the applicability of this correlation to fluids with different Prandtl numbers remains uncertain.
Experimental works have also explored channels with unconventional cross-sectional shapes and non-straight geometries, thanks to the previously discussed design freedom in additive manufacturing. Wildgoose and Thole [52] performed an experimental and numerical investigation of the thermal and hydraulic performance of various cross-sectional channel geometries. Among the tested shapes, the pentagon was identified as the optimal compromise between heat transfer enhancement and pressure drop. The study also highlighted the need to identify an alternative scaling parameter, rather than the hydraulic diameter, to better capture the flow behavior induced by complex cross-sections. Kirsch and Thole [31] tested wavy microchannel coupons with different wavelengths. Compared to a straight DMLS channel, the wavy channels with longer wavelengths exhibited significantly higher heat transfer augmentation for a similar friction factor augmentation, especially at low Reynolds numbers ($Re < 4000$), whereas the shorter-wavelength channel showed a much higher friction factor due to flow separation. These results showcase the endless possibilities of AM in designing innovative cooling channels, enhancing heat transfer despite roughness challenges. Further studies are therefore needed to better understand and predict these roughness effects across a wider range of conditions, beyond the correlation proposed by Stimpson (Equation 2).
An example of such research is the work by Soares [44], who investigated heat transfer in AM circular channels using water with varying Prandtl numbers. Unlike the discussed works, her experimental setup allowed the Prandtl number to be varied by changing the water temperature. This made it possible to investigate how AM-induced roughness influences heat transfer when fluid properties vary significantly. The main finding was that, with high relative roughness, increasing the Prandtl number appeared to reduce heat transfer performance, in contrast to classical theory. Her work, conducted with a previous version of the experimental rig used in this study, was the starting point for this thesis.
It must be noted that the additive manufacturing process strongly influences surface roughness and, therefore, its impact on pressure drop and heat transfer [43]. This implies that comparing results across different test objects and formulating general predictive correlations may be challenging when significant variations in printing parameters and materials are present. Hence, identifying general roughness parameters that effectively characterize AM surfaces is essential [30]. To achieve this, preliminary experimental works [33] [24] have investigated at the local scale, using upscale artificial roughness plates, how surface roughness affects flow structures and heat transfer mechanisms. While the friction factor has shown a significant dependence on the roughness parameter R_z [33], this parameter cannot fully describe the convective heat transfer, and other parameters, such as the frontal solidity, have been proposed [24]. However, research is still far from fully understanding these phenomena, as experimental studies struggle to generalize roughness effects.

1.5.3 CFD Analysis

Computational fluid dynamics (CFD) simulations provide a valuable tool to better understand and characterize the local effects of AM-induced roughness on the flow and heat transfer. Garg *et al.* [19] analyzed fully developed turbulent air flow (at $Re = 8000$) in circular pipes with AM-induced roughness, varying height and skewness, using wall-resolved LES with uniform wall heat flux. To generate the mesh, a rectangular portion of an additively manufactured downskin surface was mapped using an optical high-resolution microscope and a

scanning electron microscope. The roughness height was then rescaled to produce six cases while preserving the surface pattern (and flipped to obtain negative skewness). The channel geometry was created by mirroring the planar rough surface along the x-axis, then rotating it around the same axis, and merging the points along the closing line using a custom code. For a given roughness height, skewness was found to change the equivalent sand-grain roughness. It was also observed that windward peaks intensify mixing, enhancing momentum and heat transfer, while recirculation zones behind the crests act as thermal resistances, reducing local heat flux more than momentum transfer. This reveals a decoupling between momentum and heat transfer, challenging the Reynolds analogy, in agreement with results obtained for other roughness types [14]. In a similar work, Garg *et al.* [20] analyzed fully developed air flow in circular pipes at four mean roughness heights and five Reynolds numbers ranging from 1000 to 18000, using again wall-resolved LES with uniform wall heat flux. A deviation between momentum and heat transfer was observed in this study as well; however, a clear correlation was found between roughness height and global heat transfer, with higher roughness levels yielding greater enhancement. The correlation proposed by Stimpson (Equation 2) was assessed and found to significantly underestimate the Nusselt number for $Re > 6000$, highlighting the need for refined correlations. Analysis of the probability density functions (PDFs) of the local Stanton number showed that both Reynolds number and roughness intensity modulate local heat transfer behavior in a nonlinear way. The already mentioned recirculation zones, where the local Stanton number is lower than the average, in general occupy a much larger fraction of the surface than the windward peaks of elevated St, resulting in a long right-hand tail of the PDF. While contributing to the understanding of heat transfer mechanisms over AM-induced rough surfaces, these works strongly highlight the need for further investigations to develop new correlations for more accurate predictions and to enhance the general understanding of the phenomenon.

2. Theoretical background

This chapter provides an overview of the fundamental physical concepts necessary to understand the work presented in this thesis. To achieve this, the principles of convective heat transfer are presented. In addition, the classical roughness model and the specific characteristics of roughness induced by additive manufacturing are discussed.

2.1. Fundamental Concepts

2.1.1 Governing Equations

The analysis of convective heat transfer starts with the fundamental balance equations of continuum mechanics (conservation of mass, momentum, and energy) for a fluid element. These equations are presented here in their general vector form, followed by the simplifying assumptions relevant to the present work.

Mass conservation: The continuity equation expresses the conservation of mass in a flow field [1]:

$$\frac{D\rho}{Dt} + \rho\nabla \cdot \mathbf{v} = 0 \tag{3}$$

where $\mathbf{v} = (u, v, w)$ is the velocity vector and $\frac{D}{Dt} = \frac{\partial}{\partial t} + (\mathbf{v} \cdot \nabla)$ is the total derivative in time, which accounts local $(\partial/\partial t)$ and convective contributions $(\mathbf{v} \cdot \nabla)$. Under the incompressible flow assumption, the equation reduces to:

$$\nabla \cdot \mathbf{v} = 0 \tag{4}$$

Momentum conservation: The application of Newton's second law to a fluid element leads to the Navier–Stokes equations [1] :

$$\rho\frac{D\mathbf{v}}{Dt} = -\nabla p + \mu\nabla^2\mathbf{v} + \rho\mathbf{g} \tag{5}$$

where $-\nabla p$ represents the pressure gradient force, $\mu\nabla^2\mathbf{v}$ the viscous stresses, and $\rho\mathbf{g}$ the body forces (gravity). Under steady-state conditions, forced convection, and incompressible flow assumption, it reduces to:

$$\rho(\mathbf{v} \cdot \nabla)\mathbf{v} = -\nabla p + \mu\nabla^2\mathbf{v} \tag{6}$$

Energy conservation: The first law of thermodynamics for a moving fluid element, with the hypothesis of constant c_p, can be written as [1]:

$$\rho c_p\frac{DT}{Dt} = \nabla \cdot (\lambda\nabla T) + q''' + \mu\Phi \tag{7}$$

where λ is the thermal conductivity, q''' the volumetric heat generation rate, and $\mu\Phi$ the viscous dissipation term. The term $\nabla \cdot (\lambda \nabla T)$ represents the diffusion of heat due to conduction according to Fourier's law. For an incompressible fluid with constant properties, no internal heat generation, and steady-state conditions, the energy equation simplifies to:

$$\rho c_p (\mathbf{v} \cdot \nabla) T = \lambda \nabla^2 T + \mu \Phi. \tag{8}$$

Although these governing equations are not directly solved in the present work, they provide the theoretical foundation for the introduction of the dimensionless groups and correlations employed in the following sections.

2.1.2 Laminar Boundary Layer Flow

The Navier-Stokes and energy equations admit analytical solutions only for a very limited number of highly idealized problems. Prandtl's boundary layer theory provides a framework to simplify the governing equations by recognizing that viscous effects are confined to a thin region adjacent to the wall, while the outer flow is treated as inviscid and undisturbed [1]. Figure 2 illustrates the development of the momentum and thermal boundary layers over a flat plate.

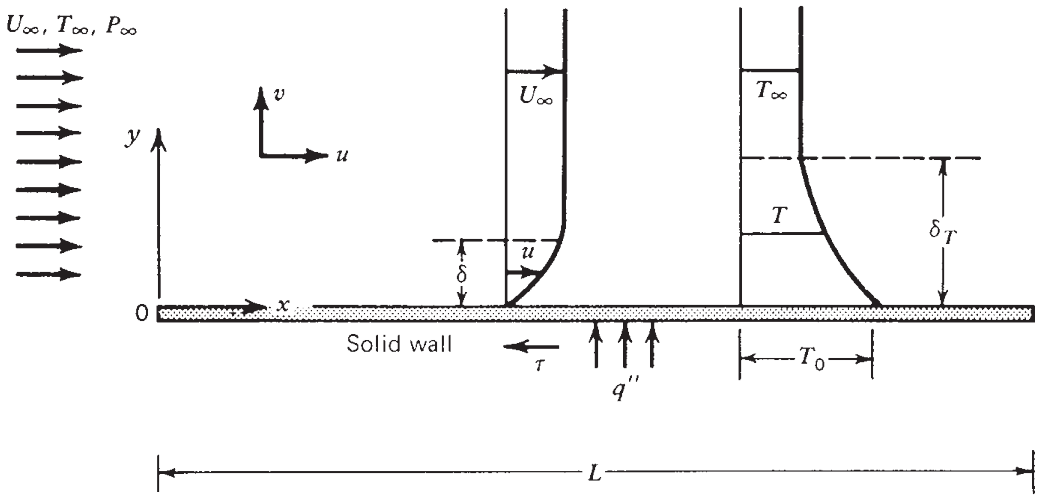

Figure 2: boundary layer over flat plate [1]

For the case of incompressible uniform flow over a flat plate with zero pressure gradient, the simplification leads to the boundary layer formulation with to the following conditions:

- At the leading edge ($x = 0$): uniform velocity $u = U_\infty$, $T = T_\infty$
- At the wall ($y = 0$): $u = 0$ (no slip condition), $T = T_w$
- Far from the wall ($y \to \infty$): $u \to U_\infty$, $T \to T_\infty$

Under these assumptions, the boundary layer approximation reduces the momentum equation to [1]:

$$u\frac{\partial u}{\partial x} + v\frac{\partial u}{\partial y} = \nu\frac{\partial^2 u}{\partial y^2} \tag{9}$$

and the thermal energy equation to:

$$u\frac{\partial T}{\partial x} + v\frac{\partial T}{\partial y} = \alpha\frac{\partial^2 T}{\partial y^2} \tag{10}$$

By estimating the relative magnitude of inertia and viscous terms in the boundary-layer momentum equation, it is obtained the scaling relation [1]:

$$\frac{\rho U_\infty^2}{L} \sim \frac{\mu U_\infty}{\delta^2} \tag{11}$$

This relation can be rearranged to give:

$$\frac{\delta}{L} \sim \left(\frac{\nu}{U_\infty L}\right)^{1/2} \tag{12}$$

Introducing the Reynolds number:

$$Re = \frac{U_\infty L}{\nu} \tag{13}$$

which measures the ratio of inertial to viscous forces in the flow. Therefore:

$$\frac{\delta}{L} \sim Re^{-1/2} \tag{14}$$

In the same way, by comparing the convection and diffusion terms in the energy equation it is found [1]:

$$u\frac{\Delta T}{L} \sim \alpha\frac{\Delta T}{\delta_T^2} \tag{15}$$

where $\alpha = k/(\rho c_p)$ is the thermal diffusivity. For fluids with $Pr > 1$, the thermal boundary layer is thinner than the velocity boundary layer ($\delta_T < \delta$). In this case the velocity scale inside δ_T can be estimated as [1]:

$$u \sim U_\infty \frac{\delta_T}{\delta} \tag{16}$$

Substituting into the convection to diffusion balance and using Equation 12, gives:

$$\frac{\delta_T}{\delta} \sim Pr^{-1/3} \tag{17}$$

where the Prandtl number is defined as

$$Pr = \frac{\nu}{\alpha} = \frac{c_p \mu}{\lambda_f} \tag{18}$$

With $Pr > 1$, the thermal boundary layer is thinner than the momentum boundary layer, since momentum diffuses faster than heat.
Along with Reynolds and Prandtl numbers, which govern the relative importance of inertia, viscosity and thermal diffusion, it is convenient to introduce a third dimensionless group, the Nusselt number, that directly quantifies the heat transfer rate between the wall and the fluid.
According to Newton's law of cooling:

$$q_s'' = h(T_w - T_\infty) \tag{19}$$

where h is the heat transfer coefficient. At the wall, due to the no-slip condition, heat is transferred by conduction, described by Fourier's law:

$$q_s'' = -\lambda_f \left.\frac{\partial T}{\partial y}\right|_{y=0} \tag{20}$$

Combining the two expressions:

$$h = -\frac{\lambda_f}{T_w - T_\infty} \left.\frac{\partial T}{\partial y}\right|_{y=0} \tag{21}$$

Introducing the nondimensional temperature:

$$\theta = \frac{T - T_\infty}{T_w - T_\infty} \tag{22}$$

the local Nusselt number is obtained as:

$$Nu_x = -x \left.\frac{\partial \theta}{\partial y}\right|_{y=0} = \frac{hx}{\lambda_f} \tag{23}$$

with x the distance from the leading edge along the plate. The Nusselt number expresses the dimensionless temperature gradient at the wall, and provides a direct measure of the intensity of convective heat transfer relative to pure conduction. For a laminar boundary layer on a flat plate, the solution of the coupled momentum and energy equations gives the classical result $Nu_x \sim Re_x^{1/2} Pr^{1/3}$ [1].
These concepts are derived for the laminar regime, when the boundary layer flow remains orderly. It is common knowledge that when the Reynolds number increases beyond a critical value, the flow becomes unstable and gradually transitions to turbulence.

2.1.3 Turbulent Boundary Layer Flow

Once transition has occurred, the boundary layer becomes turbulent and the flow field is characterized by strong, irregular fluctuations in both velocity and temperature. Despite their apparent randomness, turbulent flows have coherent eddies of various sizes, which strongly enhance the transport of momentum and energy. In the near-wall region, due to the no slip condition, a thin viscous sublayer exists, where momentum and heat transfer

are governed primarily by molecular diffusion. In Figure 3, the evolution from laminar to turbulent boundary layer over a flat plate is shown.

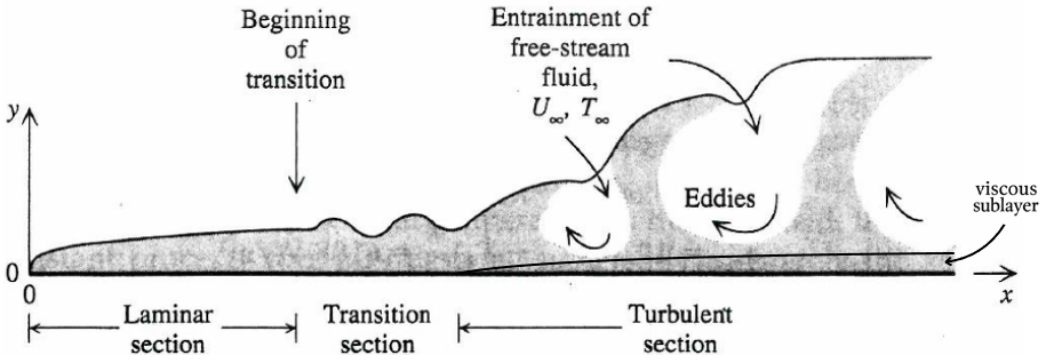

Figure 3: evolution of the boundary layer over flat plate

The Navier-Stokes and energy equations are the governing equations even for the turbulent boundary layer, but their direct solution in instantaneous form is not feasible. Therefore, the velocity and temperature fields are decomposed into mean and fluctuating components according to the Reynolds decomposition [1]:

$$u_i = \overline{u_i} + u_i' \qquad T = \overline{T} + T' \tag{24}$$

where the overbar denotes a time-averaged quantity and the prime denotes a fluctuation.
Substituting this decomposition into the Navier–Stokes equations and applying the time average leads to the Reynolds-averaged equations of motion [1]:

$$\rho\left(\overline{u_j}\frac{\partial \overline{u_i}}{\partial x_j}\right) = -\frac{\partial \overline{p}}{\partial x_i} + \mu\frac{\partial^2 \overline{u_i}}{\partial x_j^2} - \frac{\partial}{\partial x_j}\left(\rho\,\overline{u_i' u_j'}\right). \tag{25}$$

The additional term $-\rho\,\overline{u_i' u_j'}$ represents the so-called Reynolds stresses, which account for the transport of momentum by turbulent fluctuations. The same procedure applies to the energy equation, introducing the turbulent heat flux term.
These terms reflect the physical effect of turbulence: the transport of momentum and energy is dominated by the mixing action of turbulent eddies. As a result, wall shear stress and heat flux are considerably higher than in laminar flow. The presence of the turbulent transport terms makes it impossible to derive closed-form analytical solutions of the governing equations in the turbulent regime. For this reason, practical predictions of friction factors and heat transfer coefficients rely on empirical correlations derived from systematic experiments. These correlations are not arbitrary: they are guided by dimensional analysis, in particular by the Buckingham Π theorem [50], which provides the theoretical basis for expressing complex transport phenomena in terms of a limited number of dimensionless groups. In convective heat transfer, this approach leads to correlations of the general form:

$$Nu = f(Re, Pr, \dots) \tag{26}$$

where, for turbulent internal flows, the friction factor is also included in the functional dependence, highlighting the close connection between momentum and heat transfer mechanisms. Such correlations allow the generalization of convective behavior across different fluids, geometries, and flow conditions.

2.2. Duct Flow

The concepts introduced for external boundary layers apply directly to internal flows, with the boundary layer growing in the streamwise direction. The main difference with respect to flow on a flat plate is that in ducts, the boundary layers developing from the walls merge at the centerline, after which the flow no longer changes its shape along the duct; this condition is named fully developed flow, while the region where the boundary layers are developing is called the entrance region. In Figure 4 the development of the thermal boundary layer inside a circular tube is shown.

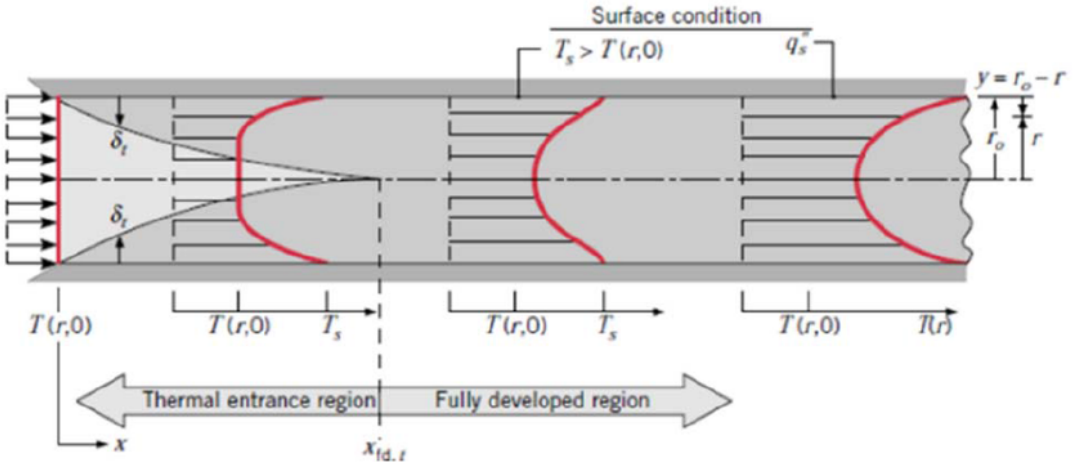

Figure 4: thermal boundary layer inside a circular tube [21]

Also in duct flows, the dimensionless groups Re and Pr are used to characterize the flow regime and the relative development of velocity and thermal boundary layers. In this case, the Reynolds number is defined as [50]:

$$Re = \frac{\rho u D_h}{\mu} \tag{27}$$

where u is the bulk velocity and D_h is the hydraulic diameter, defined as $D_h = 4A_c/P$, with A_c the cross-sectional area and P the wetted perimeter. For a circular duct, the hydraulic diameter reduces to the actual diameter, $D_h = D$. As for the flat plate, the flow regime in internal ducts depends on the Reynolds number, and the thresholds commonly accepted are [50]:

- $Re < 2300$: Laminar flow
- $2300 < Re < 4000$: Transitional flow
- $Re > 4000$: Turbulent flow

The onset of turbulence varies across sources due to the inherent ambiguity of the transitional regime. Moreover, the critical Reynolds at which the transition starts can vary depending on factors such as surface roughness and inlet conditions [50] [30].
The hydrodynamic entrance length relative to the diameter of the pipe, function of the Reynolds number, is given as follows [50]:

- $L_e/D \approx 0.06Re$ for laminar flow
- $L_e/D \approx 4.4Re^{1/6}$ for turbulent flow

While the thermal entrance length, relative to the diameter of the pipe, is given as follows [29]:

- $L_e/D \approx 0.05RePr$ for laminar flow
- $10 \lesssim L_e/D \lesssim 60$ for turbulent flow (usually assumed fully developed at $L/D > 10$)

The thermal entrance length is longer than the velocity one in the case of liquid water. This is because, under any condition, the Prandtl number is greater than 1, which leads to a slower development of the thermal boundary layer. In the entrance region, the heat transfer coefficients are considerably higher than in the fully developed regime and various corrections to analytical solutions and experimental correlations were proposed. However, for sufficiently long ducts ($L/D \gg 60$) entrance effects become negligible and the flow can be treated as fully developed [29].

2.2.1 Friction Factor

In fully developed duct flow, the mean pressure gradient is balanced by the wall shear stress [1]. The wall shear stress is given by:

$$\tau_w = \mu \left.\frac{\partial u}{\partial y}\right|_{y=0} \tag{28}$$

and represents the tangential stress acting at the wall due to viscosity.
A dimensionless group, the Darcy friction factor, is introduced, defined as [50]:

$$f_D = \frac{8\tau_w}{\rho u^2} \tag{29}$$

The corresponding pressure drop over a duct of length L is obtained from the Darcy–Weisbach relation [50]:

$$\Delta p = f_D \frac{L}{D_h} \frac{\rho u^2}{2} \tag{30}$$

The Darcy friction factor f_D should not be confused with the Fanning friction factor, or skin-friction coefficient, defined as:

$$C_f = \frac{\tau_w}{\frac{1}{2}\rho u^2} = \frac{f_D}{4} \tag{31}$$

The friction factor depends on the relative roughness and the Reynolds number, with different trends depending on the flow regime, as shown in the Moody diagram.

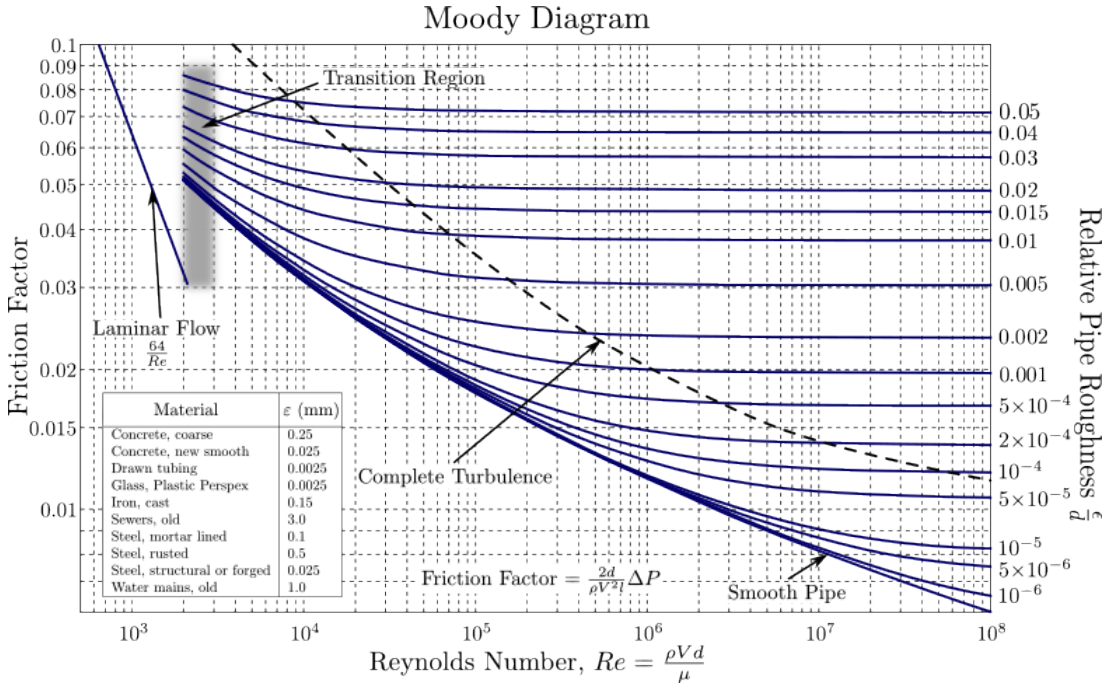

Figure 5: Moody diagram [51]

f_D is derived analytically for the laminar regime, resulting in the Hagen–Poiseuille solution[50]:

$$f_D = \frac{64}{Re} \tag{32}$$

While for the turbulent regime, empirical correlations are needed.
The most used is the Colebrook-White [50]:

$$\frac{1}{\sqrt{f_D}} = -2\log_{10}\left(\frac{\epsilon/D}{3.7} + \frac{2.51}{\mathrm{Re}\sqrt{f_D}}\right) \tag{33}$$

As also demonstrated by Nikuradse's experiments [38], while the Darcy friction factor in laminar flow depends only on the Reynolds number, relative roughness plays a critical role in determining the friction factor in turbulent flow. When the roughness is submerged within the viscous sublayer, it has no impact on the friction factor, and the pipe is considered hydraulically smooth. When the relative roughness significantly exceeds the thickness of the viscous sublayer, the friction factor becomes independent of the Reynolds number, and the flow is classified as fully rough, with the friction factor as a function of the roughness. The Colebrook-White effectively combines the effects of smooth and fully rough flows, providing a comprehensive model for the turbulent friction factor.

2.2.2 Heat Transfer

For an internal flow, the absence of a fixed free stream temperature necessitates using a mean, or bulk, temperature that varies in the direction of the flow [29]. Therefore, Newton's law of cooling has to be expressed, replacing T_∞ with T_b, as [29]:

$$q_s'' = h_{loc}(T_w - T_b) \tag{34}$$

where h_{loc} is the local heat transfer coefficient. However, in the thermally fully developed flow of a fluid with constant properties, the local heat transfer coefficient is a constant, therefore equal to the average one. To predict the heat transfer coefficient, as said in the previous section, relations between dimensionless groups are used. For an incompressible fluid in a smooth circular tube, analytical solutions of the boundary layer equations are applicable for laminar flow, while empirical correlations are needed in the turbulent regime. The laminar solution is independent of the Re and depends only on the thermal boundary condition [29]:

- $Nu = 3.66$ for constant surface temperature
- $Nu = 4.36$ for constant heat flux

For turbulent flow, two main correlations are used [29]. The Dittus-Boelter:

$$Nu = 0.023 Re^{0.8} Pr^{n} \tag{35}$$

Where $n = 0.3$ when the fluid is cooled by the tube wall and $n = 0.4$ when the fluid is heated by the tube wall. It is valid for $Re > 10000$ and typically has an error of approximately 25%.
And the Gnielinski correlation, more recent and complex, expressed as:

$$Nu = \frac{\left(\frac{f_D}{8}\right)(Re - 1000)Pr}{1 + 12.7\left(\frac{f_D}{8}\right)^{0.5}\left(Pr^{2/3} - 1\right)} \tag{36}$$

It includes the Darcy friction factor f_D, that can be obtained from the Moody diagram or calculated using the Colebrook-White equation as seen in section 2.2.1. It is applicable for $Re > 3000$ and generally has an error of less than 15%.
These correlations are valid for thermally fully developed flow, and, as said, it may be necessary to take into account the effect of the entry region with proper corrections.
Table 1 summarizes the principal dimensionless groups used throughout this chapter and in the experimental analysis. The characteristic length L_c for all dimensionless groups except the Biot number corresponds, in the case of convection inside a pipe, to the hydraulic diameter of the pipe. For the Biot, L_c must be defined for each specific case, as it depends on the solid body being analyzed.

Table 1: Dimensionless groups in convective heat transfer

Group	**Definition**	**Interpretation**
Biot number (Bi)	$\frac{hL_c}{\lambda_s}$	Ratio of the internal thermal resistance of a solid to the boundary layer thermal resistance.
Darcy friction factor (f_D)	$\frac{\Delta p}{(L/D)(\rho u^2/2)}$	Dimensionless pressure drop for internal flow.
Fanning friction factor (C_f)	$\frac{2\tau_w}{\rho u^2}$	Dimensionless surface shear stress.
Nusselt number (Nu)	$\frac{hL_c}{\lambda_f}$	Dimensionless temperature gradient at the wall.
Peclet number (Pe)	$Re \cdot Pr = \frac{uL_c}{\alpha}$	Ratio of advection to conduction heat transfer rates.
Prandtl number (Pr)	$\frac{\nu}{\alpha} = \frac{c_p \mu}{\lambda_f}$	Ratio of momentum diffusivity to thermal diffusivity.
Reynolds number (Re)	$\frac{\rho u L_c}{\mu}$	Ratio of the inertia to viscous forces.
Stanton number (St)	$\frac{h}{\rho u c_p} = \frac{Nu}{Re \cdot Pr}$	Modified Nusselt number.

2.2.3 Chilton-Colburn Analogy

Given the similar behavior of the velocity and thermal boundary layers, their relation and impact on global quantities, such as the friction factor and dimensionless heat transfer groups, have been investigated. The Reynolds analogy shows that, when Pr = 1, the momentum and energy equations have the same framework (Equations 9 and 10), leading to the relation [29]:

$$\frac{C_f Re}{2} = Nu \tag{37}$$

That can be rewritten as:

$$\frac{C_f}{2} = St \tag{38}$$

As demonstrated by Equation 17, the condition $Pr = 1$ ensures full alignment between the two layers. However, the analogy can be extended to a wide range of Pr (0.6 to 60) with a correction. The modified Reynolds analogy, known as the Chilton-Colburn analogy, takes the form [29]:

$$\frac{C_f}{2} = StPr^{2/3} \tag{39}$$

This important result highlights a strong link between frictional pressure drop and heat transfer for smooth surfaces. The trend of increasing h with increasing C_f remains valid for various surface roughness, but experiments [14] show that with rough surfaces, heat transfer augmentation is less effective than the friction factor augmentation. In other words:

$$\frac{C_f}{2} > StPr^{2/3} \tag{40}$$

2.3. Roughness

A brief analysis of the classical Nikuradse model for roughness is presented here, along with a distinction from the non-homogeneous roughness induced by additive manufacturing. It should be noted that, in the present work, there is no possibility to characterize roughness through detailed parameters, as this would require local experimental measurements or CFD analysis, as discussed in the previous chapter. However, it is considered essential to present the specific nature of AM-induced roughness to better understand the experimental heat transfer results.

2.3.1 Nikuradse Roughness

As already discussed in section 2.2.1, roughness influences the friction factor in turbulent flow. Nikuradse [38] provided a systematic method for studying this effect by applying uniform sand grains onto a smooth surface and measuring the resulting pressure drop as the grain height varied. These experiments allowed him to link the friction factor to a specific geometric roughness parameter, k_s, representing the height of the grains [38]. For real surfaces, which are rarely so regular (Figure 6), the concept of equivalent sand grain roughness, ϵ, is introduced [50] and used in empirical correlations, as in the Colebrook–White equation (Equation 33).

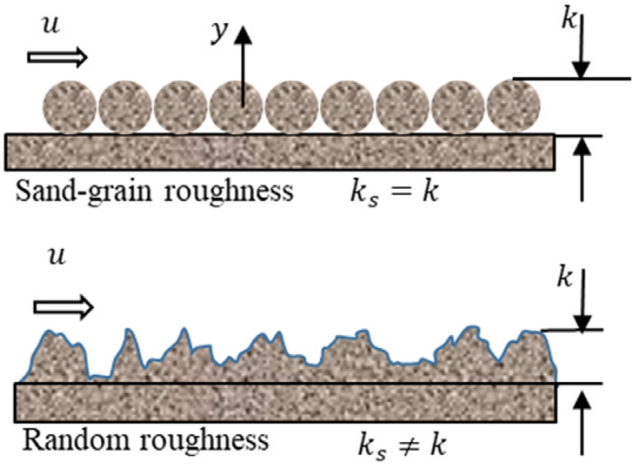

Figure 6: equivalent surface roughness [30]

While the utilization of equivalent roughness is well established for surfaces with nearly homogeneous roughness, its application to anisotropic surfaces should be approached with caution, as other parameters may be needed to better characterize the influence of roughness on flow resistance and heat transfer [30].

2.3.2 AM Roughness

The roughness induced by additive manufacturing is highly anisotropic, characterized by a chaotic distribution of peaks and valleys, as visible in Figure 7. This poorer surface quality is caused by stair-case effects (stepped texture on inclined surfaces due to layering), sag and dross formations in overhanging regions (material collapse or accumulations in unsupported areas), and powder adhesion (powder sticking to surfaces) during the layer-by-layer process [7]. The extent of these effects on roughness depends on the specific printing parameters and on the metal or alloy of the powder [12] [5].

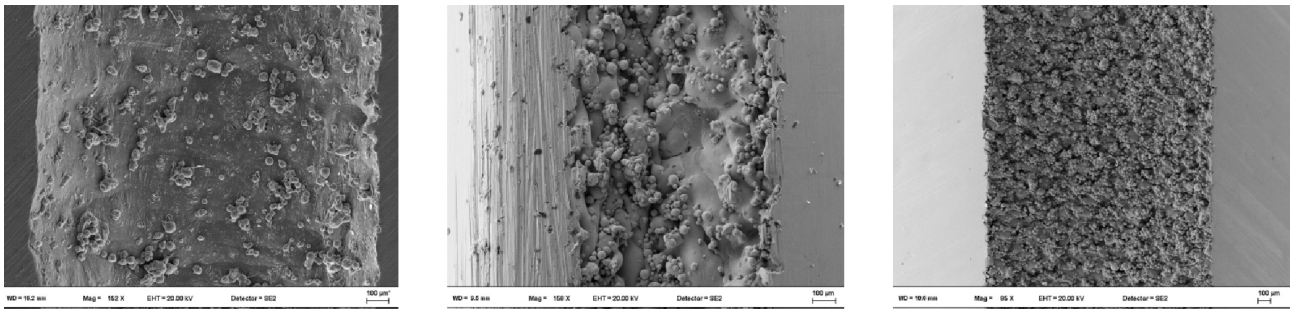

Figure 7: Aluminium, Stainless Steel and Inconel 939 AM-induced roughness

Because of this irregularity, the equivalent sand grain roughness ϵ may not adequately describe the complexity of AM surfaces [30]. This is the reason why many attempts have been made to identify alternative roughness parameters to better characterize the influence of roughness on flow resistance and heat transfer, as seen in the previous chapter.

3. Experimental Methodology

The experimental campaign aims to characterize the pressure drop and heat transfer in DMLS printed channels by determining the friction factor f_D and the Nusselt number at different flow conditions and fluid properties, characterized respectively by Reynolds number and Prandtl number. The methodology described in this chapter details the experimental setup, the tested channels, the testing procedure, the post-processing technique used to derive the dimensionless groups from raw measurements, and the uncertainty analysis.

3.1. Set Up

The rig (Figure 8) is designed to supply deionized water to the Test Object (TO) housed in the test section. The water is stored in an insulated and temperature-controlled tank. A secondary circuit draws water from the tank and sends it through one side of a plate heat exchanger, while a combined chiller/heater unit supplies the other side. A Pt100 temperature probe, immersed directly in the water tank, provides the feedback signal to the electronic controller of the unit, which uses PID regulation to achieve and maintain the desired setpoint temperature. A filter is installed in the secondary circuit to protect the heat exchanger and to improve the water and test quality. The device can operate between 5 °C and 50 °C (tank measurement) using a 50/50 water-glycol mixture, although the maximum operating temperature is limited to 42-45 °C to prevent vibration issues in the Coriolis mass flowmeter.
From the tank, water flows into two alternative supply branches, one with a variable speed low-flow pump (5–25 g/s) and the other with a fixed speed high-flow pump (300 g/s), each with its own bypass loop. Both branches merge into a single main line feeding the TO. By adjusting the bypass and main-line valves, the mass flow rate can be set to cover a wide range of conditions, allowing tests with large or small hydraulic diameters of the TO, in both laminar and turbulent regimes, providing high operational flexibility. The maximum absolute pressure achievable in the circuit is 16 bar (tested), with a safety relief valve set to open at 15 bar. The inlet and outlet temperatures and pressures of the TO are measured, along with its external surface temperature along the axial direction, using Pt100 probes.

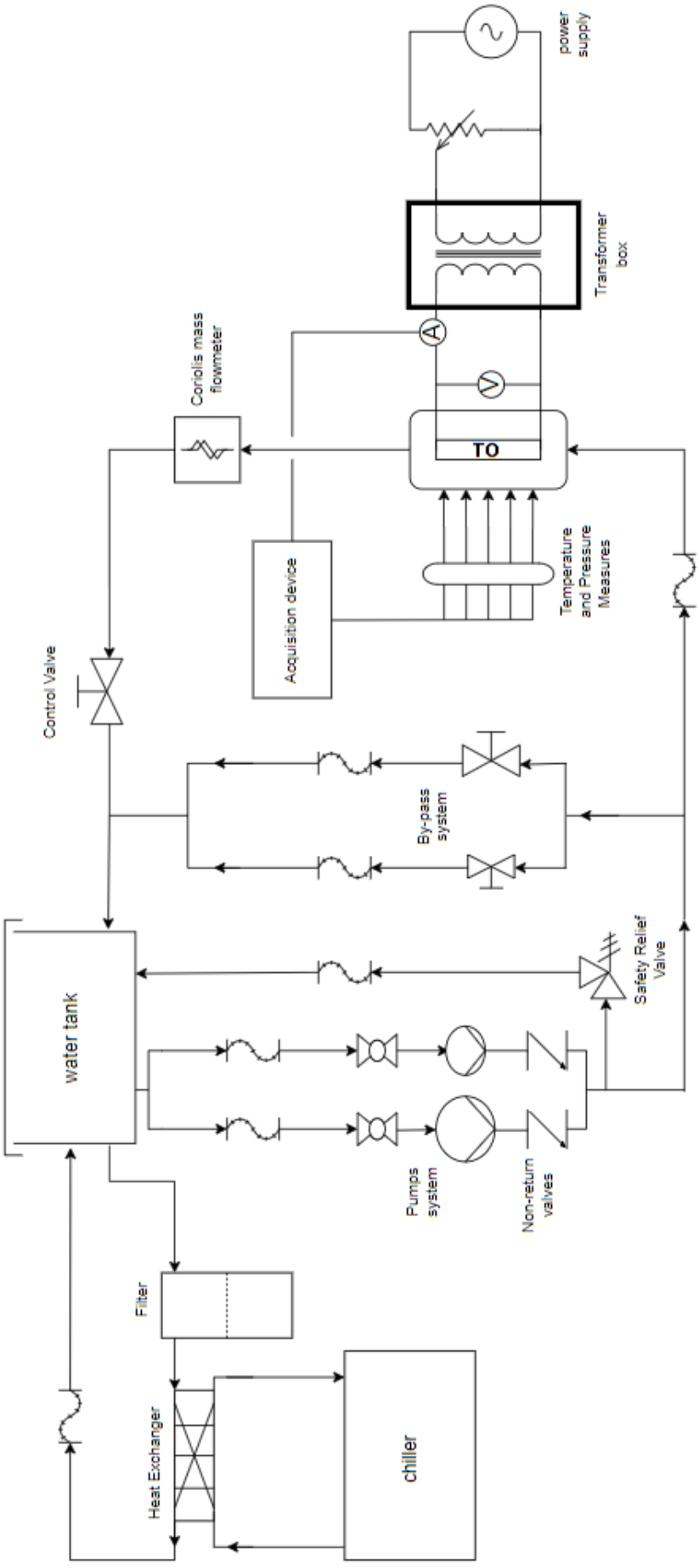

Figure 8: Layout of the experimental set-up

3.1.1 Electrical Heating

The TO, connected to the electrical heating circuit via copper clamps, is heated by Joule effect using a 50 Hz AC circuit, with electrical power regulated by adjusting the voltage through a variable autotransformer (operated with a control knob). The autotransformer is connected in series with a fixed-ratio transformer (230:2), enabling operation at very low voltages and high currents (up to 400 A). The heat generated by the Joule effect within the TO is dissipated through the cooling water and represents the thermal load for the experiments.
Figure 9 shows the electrical circuit, with two protective relays (R1 for temperature, R2 for current) that disconnect the circuit in critical conditions, and auxiliary fans for cooling the electrical system.

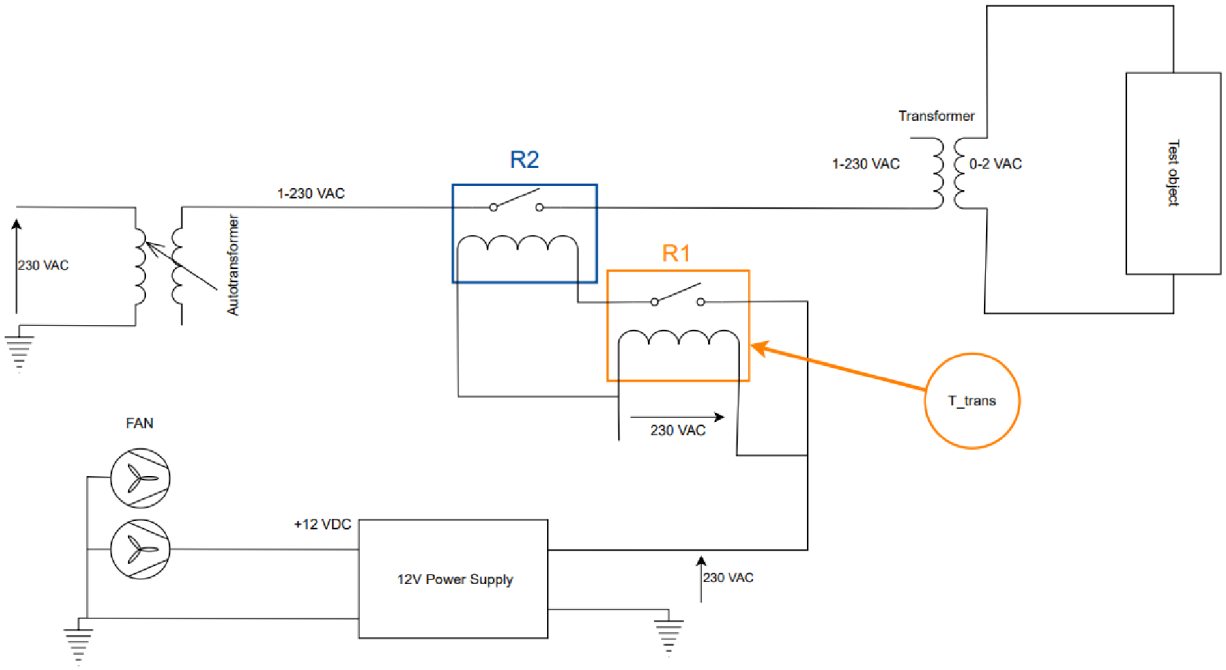

Figure 9: Layout of the electrical circuit

3.1.2 Test Section

As previously stated, the TO is connected to both the hydraulic and electrical circuits through the test section (Figure 10).

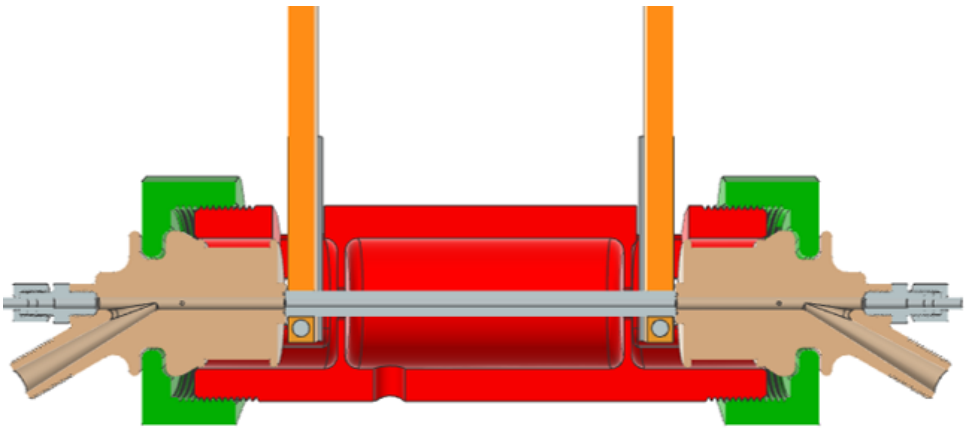

Figure 10: test section

The test section is divided into three main parts:

- The inlet and outlet caps, which connect the TO to the water circuit, house the Pentronic PT100 sensors for temperature measurements and incorporate pressure taps for pressure drop measurements (Figure 11a).
- The copper clamps, which hold the TO in place and connect it to the electrical circuit (Figure 11b);
- The test case, which provides electrical and thermal insulation for the TO (Figure 11c).

The caps and test case were custom-designed and fabricated via 3D printing, while the copper clamps were drilled in-house and reinforced with stainless-steel inserts to prevent deformation during TO replacements.

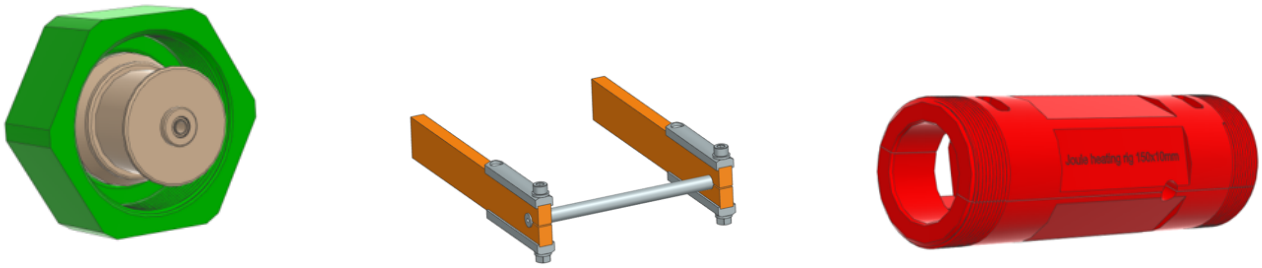

(a) Inlet cap (b) Copper clamps (c) Test case

Figure 11: components of the test section

3.1.3 Measurement System

The measurement devices used in the experimental setup are listed in Table 2.

Table 2: Measurement Devices

Device	**Physical Quantity**	**Unit**	**Range**	**Uncertainty**
Coriolis MASS2100 DI 6	Mass flow ($\dot{m}$)	g/s	0 – 75	$\left(\frac{1.372}{m} + 0.026\right)$ %
Pentronic PT100	inlet/outlet temperature	°C	0 – 200	0.05 °C
RS PT100	External surface temperature	°C	0 – 500	0.15 °C
Thermocouple type K	Copper temperature	°C	0 – 500	0.2 °C
Rosemount 3051CD4	pressure drop (Δp)	kPa	150 – 2000	1.2 kPa
Rosemount 3051CD3	pressure drop (Δp)	kPa	0 – 200	0.04 kPa

All measurement devices were provided by the laboratory and are subject to annual internal calibration. The uncertainty values reported are extracted from the respective calibration sheets. In particular, the uncertainty associated with the Coriolis was obtained by interpolating the discrete uncertainty values provided for specific mass flow rates.
The Pentronic PT100 sensors are housed in dedicated slots within the inlet and outlet caps of the test section to directly measure the temperature of the water flow. These caps also feature pressure taps, which are connected to the differential pressure transmitters via standard pressure tubing. The RS PT100 sensors are attached to the external surface of the test object (using aluminum tape) to measure its surface temperature. All sensors, except the Coriolis mass flow meter which includes its own acquisition unit, are connected to an Agilent Keysight 34972A data acquisition system for analog-to-digital signal conversion. Data are then recorded using RigView, an internal adaptation of LabView, which also provides a real-time graphical interface for monitoring parameters.

3.2. Test Objects

The Test Objects (TOs) are straight cylindrical channels with a circular section. The internal diameter varies between different TOs, while the external diameter is fixed ($D_{ext} = 10mm$), to fit precisely into the test section. Two types were used: a conventionally machined smooth channel for validation and additively manufactured (AM) channels, printed using DMLS technique. The TOs tested, along with their main characteristics, are listed in Table 3.

Table 3: Test Objects

TO Name	**Material**	**Length [mm]**	**Nominal Diameter [mm]**	**Hydraulic Diameter [mm]**	λ **[W/mK]**
Smooth	Stainless Steel	150	3.00	2.98	14
AM1	Inconel 939	90	1.50	1.37	12
AM2	Inconel 939	90	1.25	1.16	12

Inconel 939 is a nickel-based superalloy designed for high-temperature applications, offering excellent fatigue, creep, and corrosion resistance, making it ideal for additive manufacturing, especially laser powder bed fusion, due to its composition and post-processing treatments that enhance microstructure and minimize defects like porosity [40].
A noticeable reduction can be observed from the nominal (designed) to the hydraulic (actual) diameter of the AM TOs. This difference arises from challenges in accurately reproducing channels in additive manufacturing, primarily due to powder adhesion during the printing process, which reduces the diameter from the expected value [7].
Thus, for each TO, even the Smooth, the following procedure was applied to determine the hydraulic diameter. Using MATLAB, microscope images of the inlet section of the TO are analyzed. Along the contour, a sufficient number of points (typically at least 50, however increasing their number further does not change the result) are first selected by the user and then averaged by the code to generate approximately 20–25 representative nodes. This choice ensures both accuracy and repeatability, while avoiding the artificial increase of the estimated perimeter that would result from over–resolving every microscopic irregularity. The selected nodes are then interpolated with a spline to compute the enclosed area and perimeter. The procedure is repeated twice per section, proceeding in both clockwise and counterclockwise directions, and the hydraulic diameter is finally obtained from the averaged area and perimeter as $D_h = 4A_c/P$. Figure 12 shows the inlet section of a test object and the spline curve generated by the MATLAB code.

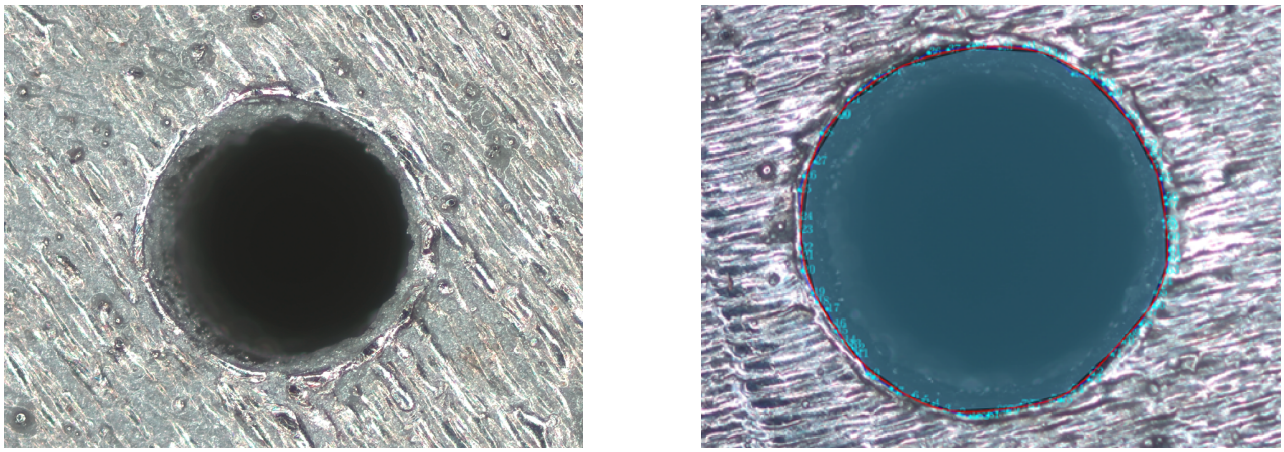

(a) microscope image of the inlet section of a TO (b) spline interpolation of the contour points

Figure 12: Hydraulic diameter evaluation through microscope analysis

This approach is inherently user-dependent, since the individual points are selected manually and it is often unclear whether a given surface irregularity should be considered or not. For this reason, the measurements

follow this fixed procedure and are repeated multiple times and averaged.

3.3. Testing Procedure

The experimental procedure for each test was as follows:

1. The TO is secured to the copper clamps by tightening the screws using a digital torque wrench to ensure consistent clamping force. Surface Pt100 probes are applied to the TO at equidistant axial positions, affixed using aluminum tape with a thin layer of thermal paste, applied between the Pt100 and the TO, to ensure thermal contact. The test section is then assembled around the TO and connected to the hydraulic circuit.
2. The high-flow pump is activated with all bypass and regulation valves fully open. The secondary circuit and the chiller/heater unit are initiated to achieve the desired temperature, which sets the Prandtl number. The entire procedure is repeated identically for different Pr values. During this phase, the pressure transmitters are purged to ensure accurate pressure measurements.
3. Once the target temperature is reached, the setup is ready to test. The high-flow pump is deactivated, and the bypass valves are closed, with only the main circuit regulation valve kept open. The low-flow pump is activated at its minimum rotational speed. By adjusting the bypass valve of the low-flow circuit, the mass flow rate through the main circuit (i.e. through the TO) is reduced until the lowest targeted Reynolds number is achieved (typically $Re = 500$).
4. Upon achieving the desired mass flow rate, the electrical circuit (the heater) is switched on, and the auto-transformer is manually adjusted with the knob to obtain a temperature difference of 4 K between the inlet and outlet of the TO. The chosen ΔT is a trade-off between ensuring sufficient measurement sensitivity and avoiding significant changes in the water properties (and consequently in the Prandtl number) within the TO. Measures (inlet and outlet temperature, pressure drop, mass flow rate and surface temperatures on the TO) are monitored in the real-time interface until visual stabilization is observed. 30 samples are then acquired at 1 Hz, with standard deviation controlled under certain thresholds, to assure stable conditions: 2% for mass flow rate and ΔP, 0.1 K for T_{in} and T_{out}, and 0.3 K for surface Pt100 probes, determined considering both the measurement uncertainties of the instrumentation and the experimental experience regarding the instability characteristics of the rig.
5. To test the next higher Re, the low-flow bypass valve is slightly closed to increase the mass flow rate, and the heater power is adjusted to restore the 4 K of ΔT. Once the bypass valve is fully closed, the flow is regulated by increasing the rotational speed of the low-flow pump until the maximum achievable mass flow rate is reached. At this point, the electrical circuit and the low-flow pump are deactivated, the high-flow bypass valve is opened and the high-flow pump is activated, using the main regulation valve and the bypass valve to adjust the flow. The electrical circuit is then reactivated, and the same testing procedure is performed.

It must be noted that the Reynolds and Prandtl numbers are calculated (as explained in the following section) in real-time based on measured quantities, allowing the operator to adjust them by modifying these quantities. For each TO, 5 different Prandtl numbers, ranging from 4 to 11, corresponding to five mean temperatures from 5°C to 42°C, as permitted by the constraints of the rig, were tested. For each Pr, as said, different Reynolds numbers were tested, covering both the laminar and turbulent regimes. Starting from $Re = 500$, they were typically spaced every 500 in the laminar regime, with closer intervals where the transition zone is expected to begin. In the turbulent regime, increments of 1000 to 2000 are used, continuing up to the limits of the rig, typically determined by system pressure approaching 15 bars or electrical circuit and TO overheating constraints.

This testing plan represents the initial intent. Achieving absolute precision in manually setting the Reynolds and Prandtl numbers was challenging. Moreover, the sequence of Re tested did not always follow the exact planned spacing, as adjustments were made depending on the diameter of the TO, due to practical issues such as flow instability and limitations in the range of the measurement instruments.

3.4. Post-Processing

For each test, the dimensionless groups were calculated from raw experimental data and water properties at mean temperature, defined as $T_m = (T_{in} + T_{out})/2$. As seen in the previous section, tests were conducted at selected Reynolds and Prandtl numbers, computed in real-time, set by adjusting the mass flow rate and water temperature.
Re was calculated rearranging its definition as function of the massflow and the hydraulic diameter:

$$Re = \frac{\dot{m} D_h}{\mu A_c} \tag{41}$$

The relevant properties, extracted from CoolProp open-source library [2], are listed in Table 4 for the five tested temperatures. Pr, being solely a function of the thermophysical properties of water, was calculated from its definition (Equation 18).

Table 4: Water Properties and Pr at different tested temperatures

T_{m} [°C]	ρ [kg/m³]	μ [mPa·s]	c_p [J/kg·K]	λ_f [W/m·K]	Pr
40.0	992	0.653	4179	0.629	4.34
26.0	996	0.870	4180	0.608	5.98
18.0	998	1.053	4185	0.594	7.41
11.0	999	1.269	4193	0.581	9.16
6.5	999	1.449	4201	0.571	10.66

The property most affected by temperature is the dynamic viscosity μ, which significantly influences the fluid dynamic behavior of water, reflected in a huge change in the Pr number.
The Friction factor f_D was calculated directly from the raw data, rearranging the Darcy-Weisbach equation (Equation 30) as:

$$f_D = \frac{2\rho D_h A_c^2 \, \Delta p}{L \dot{m}^2} \tag{42}$$

The calculation of the Nusselt number required a specific approach, since the average heat transfer coefficient could not, with this set-up, be measured or derived directly. Therefore, to determine h, a dedicated post-processing solver was developed by Brugnera [4], combining StarCCM+ simulations with custom Java and Python scripts. In its operation, the solver takes as input the experimental measurements (mass flow rate, inlet and outlet water temperatures, pressure drop, surface wall temperatures, and copper clamps temperatures) together with the geometry of the TO and the thermophysical properties of both the solid and the fluid (evaluated at T_m). The boundary conditions, shown in Figure 13, assume all walls to be adiabatic, except for parts in contact with the copper clamps, which are conductive (for this reason, their temperature is also measured). The internal channel surface is subject to forced convection from the flowing water. Joule heating in the solid of the test object is computed through the coupled electro-thermal simulation in StarCCM+.

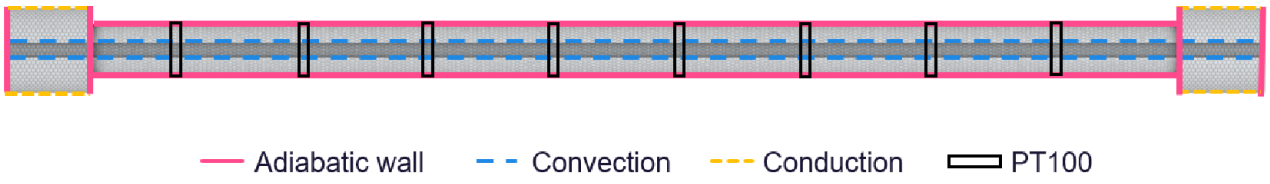

Figure 13: boundary conditions

The local energy balance for each sector i (with i denoting the axial sectors of the channel, each equipped with a PT100 sensor) is handled in the inner loop of the cycle. As an initial guess, h_{loc} is set to a fixed arbitrary value applied uniformly to each sector i; the bulk water temperature distribution is assumed linear between T_{in} and T_{out}; an arbitrary value of the voltage difference determines the Joule heating power. The simulation computes the temperature profile in the solid, including the internal wall temperature $T_{w,int}(i)$ and external wall temperature $T_{w,ext}(i)$. The water temperature is then updated along the channel using the discrete axial energy balance:

$$T_{water}(i+1) = T_{water}(i) + \frac{h_{loc}(i)\, A}{\dot{m}\, c_p} \left[T_{w,int}(i) - T_{water}(i)\right] + \frac{p(i+1) - p(i)}{\rho\, c_p} \tag{43}$$

where $T_{water}(0) = T_{in}$, and $p(i)$ denotes the pressure in i, derived from the total measured pressure drop distributed uniformly across the axial sectors.
The calculated $T_{w,ext}(i)$ are compared with the corresponding external PT100 measurements, and $h_{loc}(i)$ are iteratively adjusted using a residual-based update with a relaxation factor, until the discrepancy between the simulated and measured values falls within the prescribed tolerance.

The global energy balance is enforced in the outer loop. The simulated total heat transferred to the fluid,

$$\dot{Q}_{water,calc} = \dot{m}\, c_p\, (T_{out,calc} - T_{in}) \tag{44}$$

is computed using $T_{out,calc}$ from the axial energy balance of the inner loop and compared with the experimental value,

$$\dot{Q}_{water,real} = \dot{m}\, c_p\, (T_{out} - T_{in}) \tag{45}$$

where T_{out} is the measured value.
The volumetric Joule heating is then updated by varying the applied voltage, with a relaxation factor, in proportion to the relative difference between $\dot{Q}_{water,calc}$ and $\dot{Q}_{water,real}$, until it falls within the prescribed tolerance.
This process ensures that both local and global energy balances are satisfied, yielding the spatial distribution of the local heat transfer coefficient $h_{loc}(i)$, the bulk water temperature $T_{water}(i)$, and the internal and external wall temperatures $T_{w,int}(i)$ and $T_{w,ext}(i)$. From the local heat transfer coefficient, the average h is calculated and consequently the Nusselt number.
It is worth noting that the external surfaces of the first and last sectors are not adiabatic, as they are partially in contact with the copper clamps. The clamps provide the electrical connection but also allow some conductive heat transfer, which the simulation takes into account. The contact thermal resistance was computed with the CMY (Cooper-Mikic-Yovanovich) thermal model [10]. Even the electrical contact resistance between the copper clamps and the TO was analyzed, estimated experimentally, through voltage difference measurements, and with a resistance model [27]. The results were of the same order of magnitude and showed that the voltage difference was small compared to the total drop across the test object (for any tested condition smaller than 10%). Additionally, according to the theory [27], most of the heat generated by this resistance is conducted into the more conductive material (the copper, in this case), making its impact on the experiment negligible; its effect was therefore not considered.

3.5. Uncertainty

In this section, the uncertainty associated with both the friction factor and the Nusselt number is presented. Firstly, the methodology applied for the evaluation is described, then the results are presented.

3.5.1 Friction Factor Uncertainty

First, the total uncertainty for each direct measurement X_i is calculated by taking into account the instrumental uncertainty (type B), visible in Table 2 and the standard error of the mean (type A), as follows [36]:

$$\delta X_i = \sqrt{(\delta X_{i,\mathrm{instr}})^2 + (\mathrm{SEM}_i)^2} \tag{46}$$

The standard error of the mean is given by:

$$\mathrm{SEM}_i = \frac{\sigma_{i,\max}}{\sqrt{N}}, \quad N = 30 \tag{47}$$

where the standard deviation corresponds, in order to provide a conservative estimation, to the threshold adopted for controlling the steady-state condition.
The relative uncertainty is then computed as:

$$\delta X_i\% = \frac{\delta X_i}{\overline{X}} \times 100\% \tag{48}$$

Note that even the uncertainty of the hydraulic diameter evaluation is obtained by combining the contribution from the standard deviation of the repeated measurements and the contribution due to the instrument (the microscope) resolution:

$$\delta D_h = \sqrt{\left(\frac{\sigma}{\sqrt{N}}\right)^2 + \left(\frac{\Delta}{2\sqrt{3}}\right)^2} \quad N = 4 \tag{49}$$

The friction factor, as said, is obtained directly from the raw measurements (Equation 42). The uncertainty is therefore computed using the standard error propagation formula, assuming uncorrelated input uncertainties [36]:

$$\delta R = \sqrt{\sum_{i=1}^{n} \left(\frac{\partial f}{\partial X_i} \cdot \delta X_i\right)^2} \tag{50}$$

with $R = f_D$.
The expanded uncertainty at 95 % confidence level is then obtained by applying the coverage factor $k = 2$:

$$U_R = k \cdot \delta R, \quad k = 2 \tag{51}$$

and evaluated for the range of the Reynolds number tested and for each TO, as shown in Figure 14a.

3.5.2 Nusselt Uncertainty

For the heat transfer coefficient, which is obtained indirectly with the solver from wall temperatures, the fluid temperature difference ΔT_f (computed from inlet and outlet measurements) and the mass flow rate, the uncertainty is evaluated using the Root Sum Square (RSS) method [36], assuming statistical independence between the input quantities and under the strong assumption of local linearity of the relationship:

$$\delta h\% = \sqrt{(\delta h_{T_\mathrm{w}}\%)^2 + (\delta h_{\Delta T_\mathrm{f}}\%)^2 + (\delta h_{\dot{m}}\%)^2 + u_\mathrm{sol}^2} \tag{52}$$

The uncertainty caused by the wall temperature measurements is derived from a pre-existing limited Monte Carlo analysis at three reference Reynolds numbers, then interpolated over the range with an exponential fit. To account for the limited dataset, a conservative margin is added. Mass flow, inlet and outlet water temperature uncertainties are obtained according to Equation 46. Uncertainties of T_{in} and T_{out} are then combined in $\delta h_{\Delta T_\mathrm{f}}\%$, using the root-sum-square of their individual uncertainties. The uncertainty of the solver takes into account mesh discretization and convergence effects and is estimated as 2% (k=1) in the absence of a dedicated sensitivity analysis.
It should be noted that a more detailed assessment of the uncertainty of h would require the Monte Carlo propagation of uncertainty for every input at various Reynolds numbers [36], which was not performed due to time constraints during the laboratory work. To compute the Nu uncertainty, the RSS method is again applied, accounting for the uncertainty of the hydraulic diameter, as given in Equation 49, and the uncertainty of thermal conductivity of water is assumed fixed at 1% (k=1), as water properties are extensively studied and conductivity exhibits minimal variation with small temperature fluctuations:

$$\delta Nu\% = \sqrt{(\delta h\%)^2 + (\delta D_h\%)^2 + (u_\lambda)^2} \tag{53}$$

Finally, the expanded uncertainty at 95 % confidence level is computed and evaluated across the entire Reynolds number range tested and for each TO, as shown in Figure 14b.

3.5.3 Summary of Uncertainty Results

Figure 14 shows the trends of the uncertainty at a 95% confidence level for both the friction factor and the Nusselt number as a function of the Reynolds number for each TO. Since the uncertainty exhibits a hyperbolic dependence on *Re*, mean values for the turbulent regime, which constitutes the main region of interest in this work, have been summarized in Table 5, which reports both the expanded uncertainty (k=2) and the standard uncertainty (k=1) for each tested TO.

Table 5: Uncertainty in turbulent regime for each TO

TO	f_D		Nu	
	$k = 1$	$k = 2$	$k = 1$	$k = 2$
AM1	2.9%	5.8%	3.8%	7.6%
AM2	3.4%	6.8%	3.75%	7.5%
Smooth	1.33%	2.65%	3.7%	7.4%

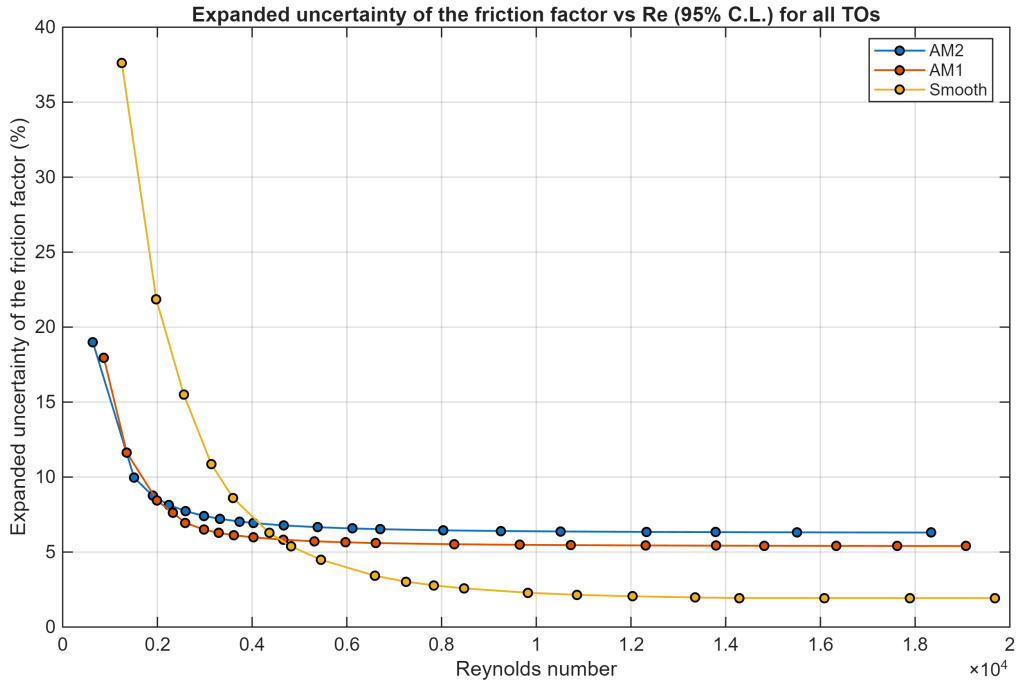

(a) Friction Factor uncertainty (95% C.L)

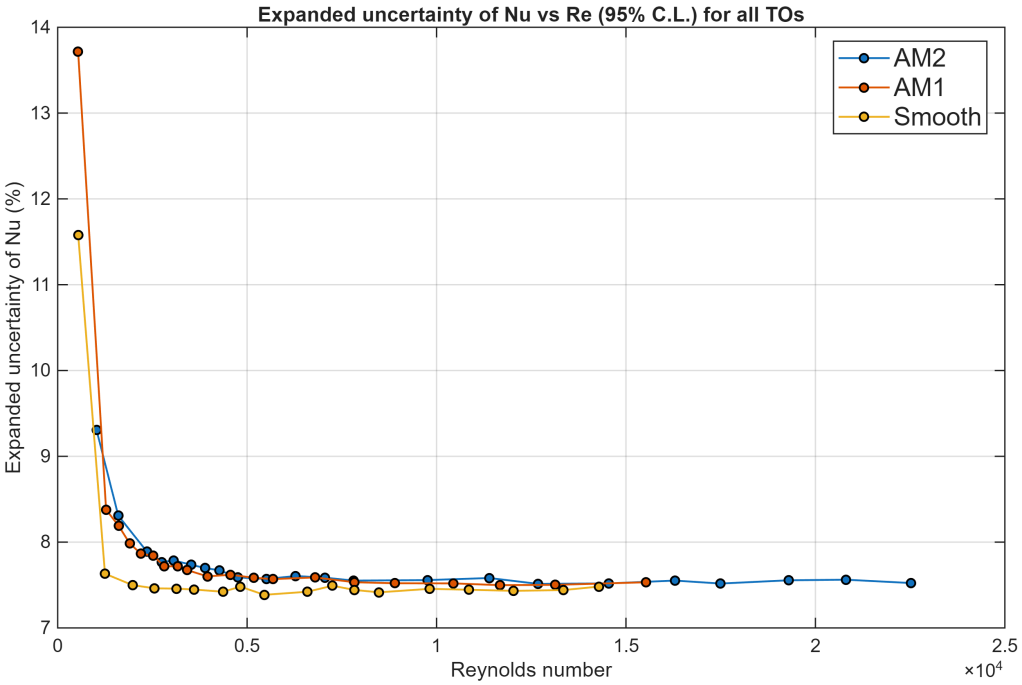

(b) Nusselt uncertainty (95% C.L.)

Figure 14: Uncertainty for each TO

In the laminar regime, the large uncertainty for the friction factor is primarily due to the Coriolis mass flow meter and the Rosemount 3051CD3, which have to operate at low flow rates and low differential pressures, thus outside their optimal measurement range. This effect is particularly evident for the smooth case, where the larger diameter, combined with the smooth surface, results in extremely low differential pressures, leading to very high uncertainty. In the turbulent regime AM1 and AM2 exhibit significantly higher uncertainty compared to the Smooth, mainly due to the evaluation of the hydraulic diameter.
For the Nusselt number, in the turbulent regime all TOs show similar uncertainty, since the hydraulic diameter has a limited influence compared to other factors such as wall temperatures, fluid temperatures and the

simulation-related uncertainty. In the laminar regime, once again, the low flow rate and the greater influence of wall temperature measurements compared to the turbulent case contribute to the higher uncertainty. As an example, for AM2, the contributions for the uncertainty of f_D and Nu are plotted in Figure 15.

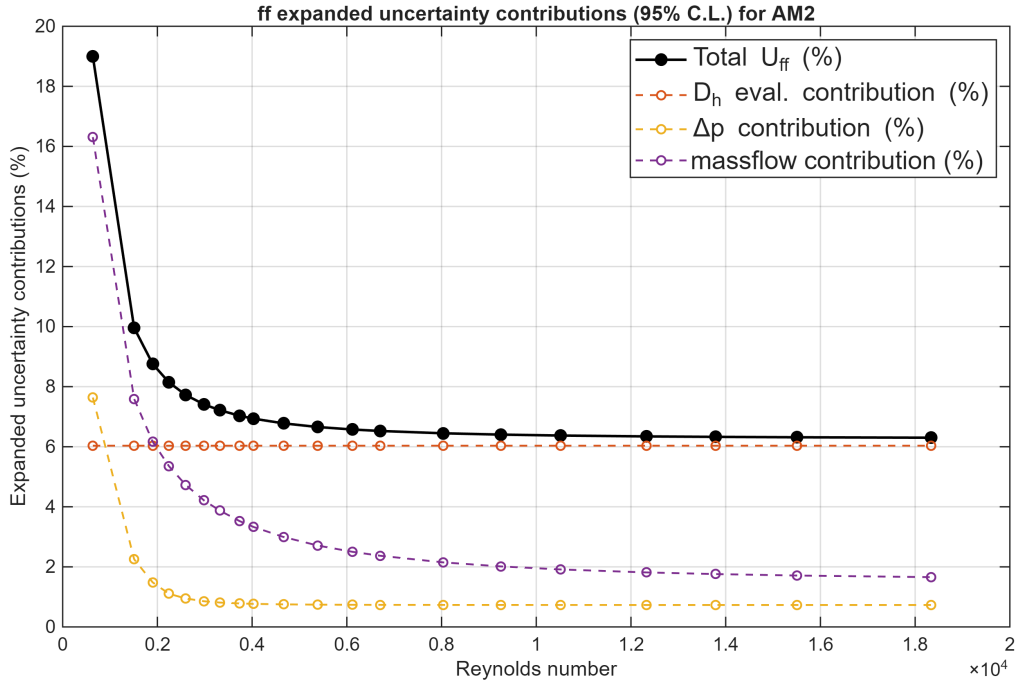

(a) Uncertainty contributions for friction factor

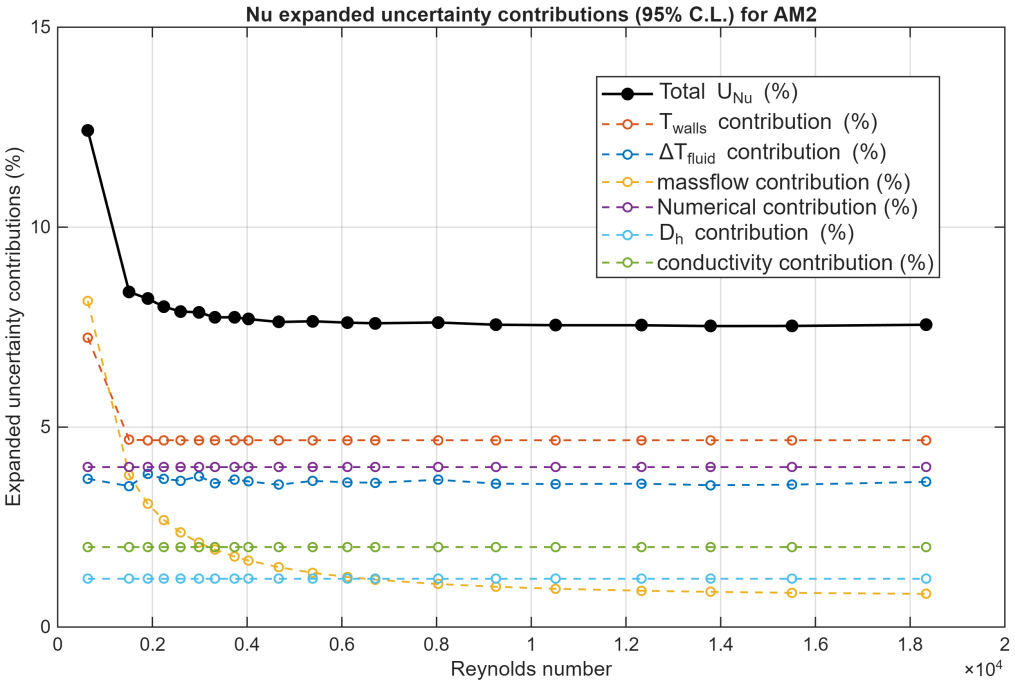

(b) Uncertainty contributions for Nusselt number

Figure 15: Uncertainty contributions for AM2

4. Results and Discussion

The experimental results for the pressure drop and heat transfer are presented in this section. Firstly, the Smooth test object results are presented as validation for the experimental setup, followed by the results for the AM printed TOs.

4.1. Validation

To validate the rig, both from a pressure drop and a heat transfer perspective, the Smooth TO was tested and its results were compared to two well-known correlations: the Colebrook–White for the friction factor and the Gnielinski for the Nusselt number. The rig was designed to operate in turbulent conditions; therefore, the measurement instruments were selected to have their optimal measurement range in this regime. Consequently, the correlations used for validation refer to the turbulent regime. The results for the laminar regime are also reported, as a first trial for the rig.

4.1.1 Friction Factor Validation

The friction factor was tested alone, without any heating, for the Smooth TO, to collect more data points (the procedure is much faster compared to that for the heat transfer coefficient).
In Figure 16, the results for the whole Reynolds number range tested (from 300 to 30000) are shown in the Moody diagram, compared to the classical correlations for laminar and turbulent regimes.

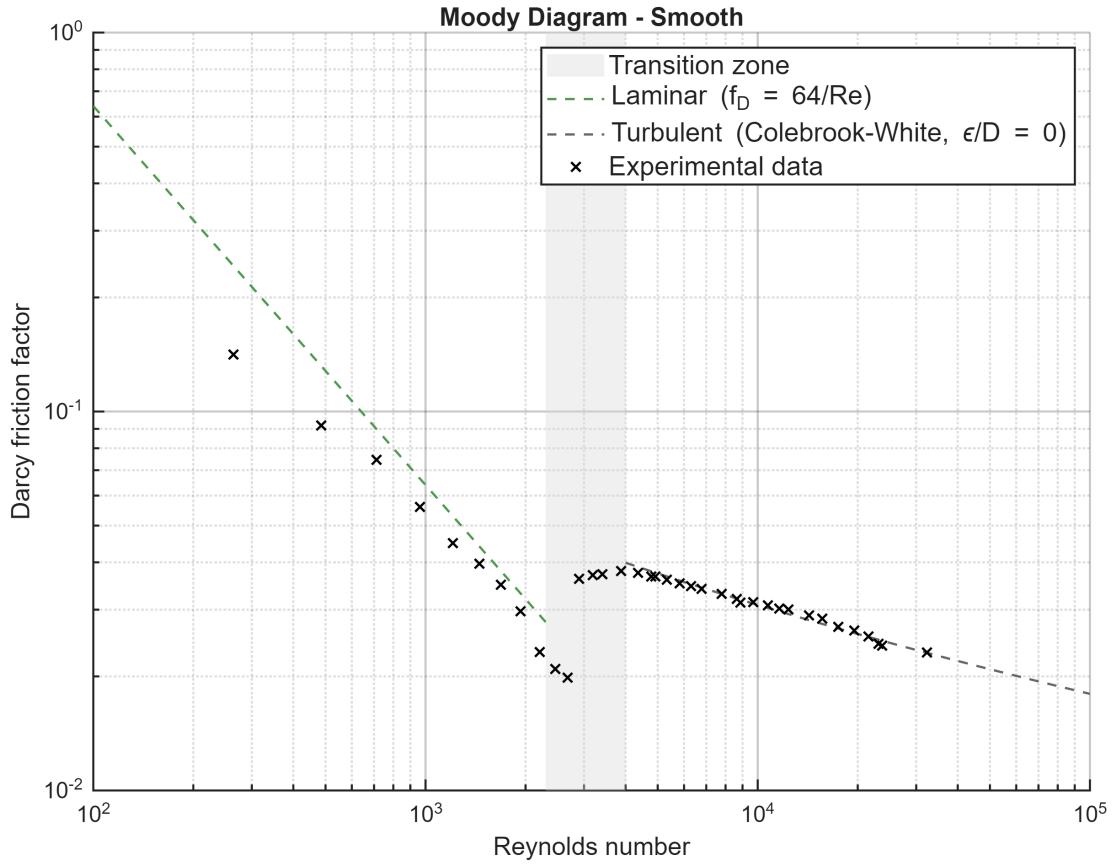

Figure 16: Friction factor for Smooth TO on the Moody diagram

A significant deviation from the theoretical expression is observed in the laminar regime. This is also evident numerically in Table 6. Such deviation is due to the high uncertainty in this regime for the Smooth TO, as shown in Figure 14a.
In Figure 17, the experimental data, with their uncertainty (Table 5), for the turbulent regime are compared to the Colebrook–White correlation. As summarized in Table 6, no bias appears to be present and the Mean

Absolute Percentage Error (MAPE) is only 1.75%. All the experimental points fall within the ±10% coverage band, confirming the excellent agreement between measurements and correlation. These results demonstrate that, from the friction factor perspective, the rig can be considered fully validated for turbulent flow conditions.

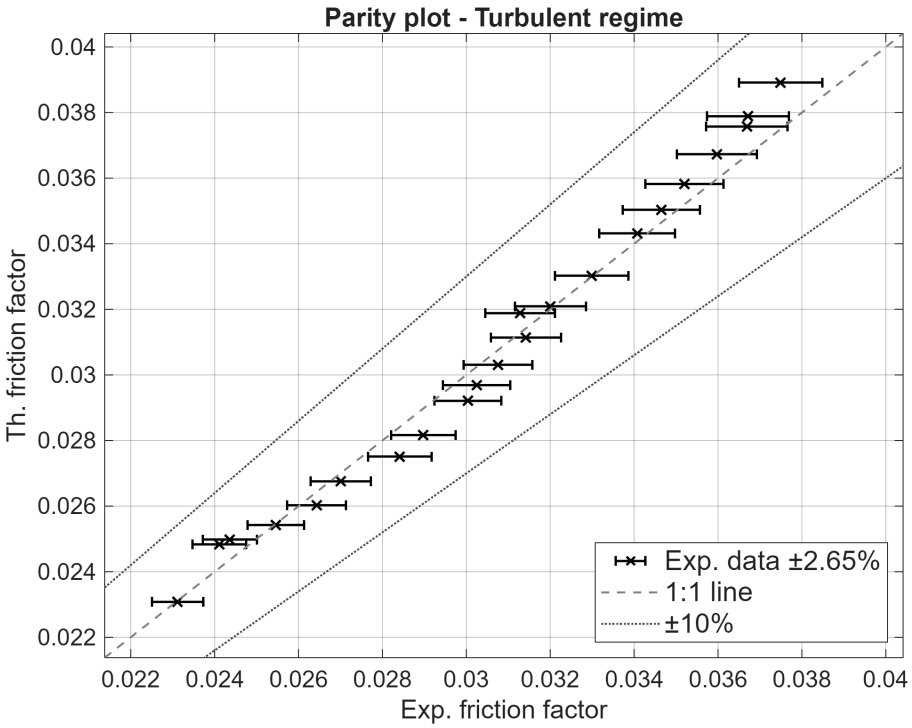

Figure 17: Parity plot of Darcy friction factor for Smooth TO in turbulent regime ($Re > 4000$)

Table 6: Error metrics in laminar and turbulent regimes for friction factor

Metric	**Regime**	
	Laminar	**Turbulent**
Bias	-0.0213	-0.000137
MAPE	18.7%	1.75%
Coverage ±10%	22.2%	100%

4.1.2 Heat Transfer Validation

For the heat transfer validation, four different Prandtl numbers were tested, increasing the Reynolds number till the limits imposed by the rig constraints. Figure 18 reports the results for Re > 3000. A clear trend can be observed: an increase in the Prandtl number corresponds to an increase in the Nusselt number, as expected and predicted by theory and correlations. In Table 7, this qualitative trend is quantified as $Nu \sim Pr^m$ with $m \approx 0.3$ for each Reynolds number. According to the Chilton–Colburn analogy (Equation 39), the expected value is $m = 1/3$, thus the observed trend is in line with theoretical expectations.

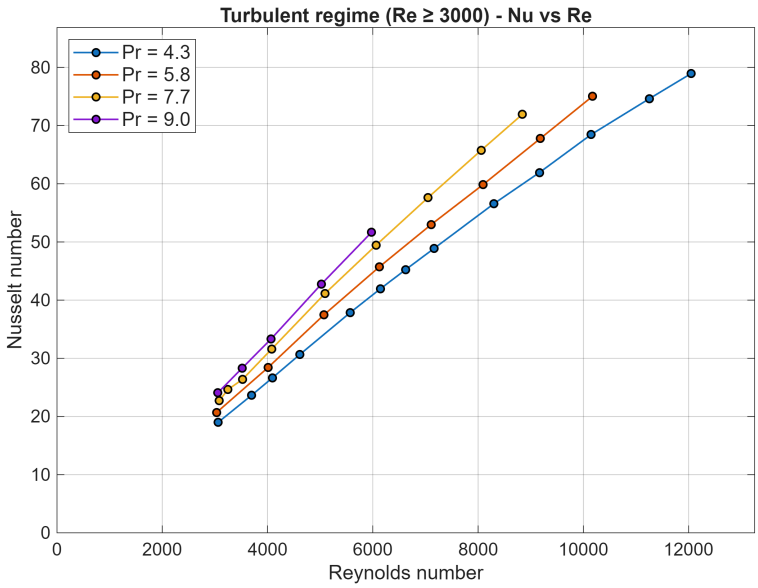

Figure 18: Nu vs Re for Smooth TO in turbulent regime

Table 7: Fit Nu $\sim$ Pr^m for Smooth TO

Re (±5%)	**Experimental dimensionless numbers**			**m**
	Re	**Pr**	**Nu**	
3000	3059	4.3	19.0	0.32
	3033	5.8	20.7	
	3081	7.7	22.7	
	3056	9.0	24.1	
4100	4091	4.3	26.6	0.31
	4008	5.8	28.4	
	4081	7.7	31.6	
	4067	9.0	33.3	
5100	5070	5.8	37.5	0.30
	5095	7.7	41.2	
	5020	9.0	42.7	
6100	6144	4.3	42.0	0.28
	6128	5.8	45.8	
	6063	7.7	49.5	
	5975	9.0	51.7	
7100	7162	4.3	48.9	0.28
	7110	5.8	53.0	
	7047	7.7	57.6	
9200	9166	4.3	61.93	0.30
	9180	5.8	67.77	
10200	10149	4.3	68.47	0.31
	10174	5.8	75.03	

To validate the rig, the Gnielinski correlation (36) was adopted as the reference model for the turbulent regime (Re $>$ 3000), applying the correction of Al-Arabi to account for entry effects [41]:

$$\frac{Nu_m}{Nu_0} = 1 + \frac{C}{L/D_h} \tag{54}$$

with Nu_0 being the Nusselt number from the Gnielinski correlation and C:

$$C = \left(\frac{L}{D_h}\right)^{0.1} \cdot Pr^{-1/6} \left(0.68 + \frac{3000}{Re^{0.81}}\right) \tag{55}$$

The parity plot in Figure 19a illustrates the comparison between experimental and predicted values for the turbulent regime, while Table 8 summarizes the corresponding error metrics. A persistent bias is observed, with the corrected Gnielinski correlation tending to overestimate the experimental results. This behavior can be attributed to the low Reynolds numbers tested. As noted by Gnielinski himself [26], his correlation tends to overpredict the Nusselt number for $Re < 10000$, where the flow is not yet fully turbulent. In this transitional range, the common approach is to interpolate between laminar and fully turbulent correlations, and several alternative models have been proposed over the years [8, 22, 26, 49]. Nevertheless, since the objective of these tests was to validate the rig, the corrected Gnielinski correlation was considered more than adequate for this purpose, being the MAPE approximately 9% and the coverage factor 97.14% within a ±15% error band.
The laminar regime results were also compared with a classical solution for finite-length tubes [25]:

$$Nu_{m,q} = \left[(Nu_{m,q1})^3 + 0.6^3 + (Nu_{m,q2} - 0.6)^3 + (Nu_{m,q3})^3\right]^{1/3} \tag{56}$$

with:

$$Nu_{m,q1} = 4.354 \tag{57}$$

$$Nu_{m,q2} = 1.953 \left(\frac{RePrD_h}{L}\right)^{1/3} \tag{58}$$

$$Nu_{m,q3} = 0.924\, Pr^{1/3} \sqrt{Re\frac{D_h}{L}} \tag{59}$$

As shown in Figure 19b, this approach appears to underestimate the experimental data. Several factors could contribute to this discrepancy, including the higher measurement uncertainty and the higher instability of the tests in the laminar regime, as well as the possible presence of turbulence promoters, such as slight surface roughness or non-ideal inlet conditions. However, the experimental data follow the general trend predicted by the correlation. Future refinements of the rig could enhance accuracy in this zone, as the rig currently operates optimally only in the turbulent range.

Table 8: Error metrics in laminar and turbulent regimes for Nusselt number

Metric	**Regime**	
	Laminar	**Turbulent**
Bias	1.253	-3.832
MAPE	11.00%	8.98%
Coverage ±15%	77.78%	97.14%

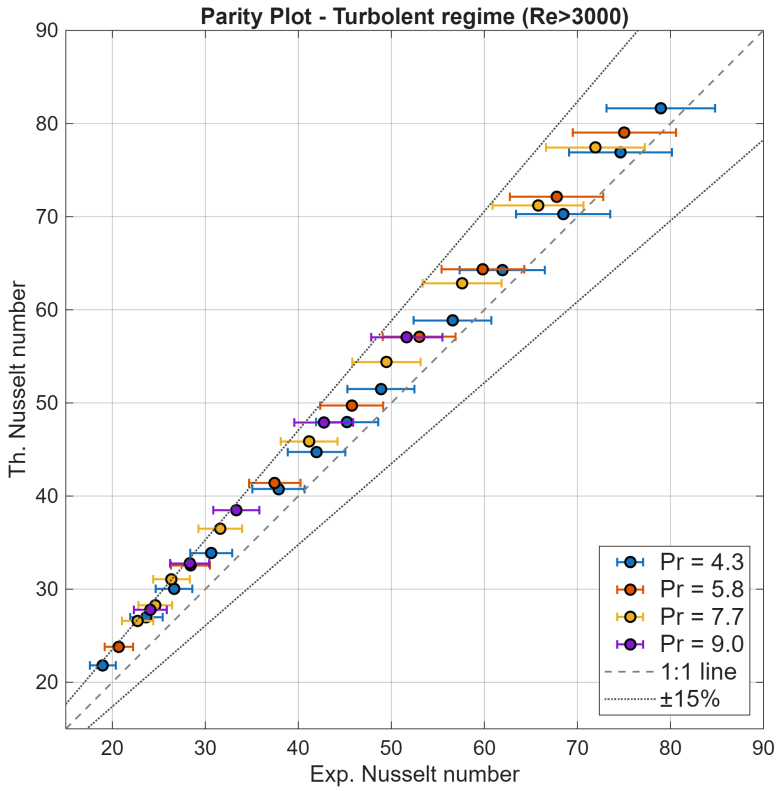

(a) Turbulent regime

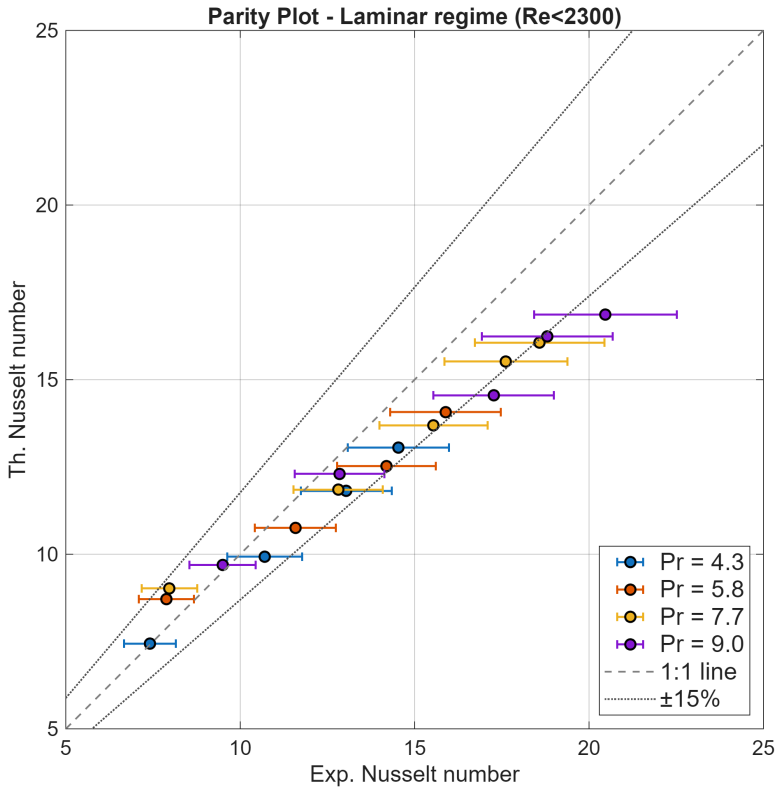

(b) Laminar regime

Figure 19: Parity plots of Nu for Smooth TO in turbulent and laminar regimes

4.2. Experimental Results for AM Channels

In this section the experimental results for the AM1 and AM2 test objects are presented. Firstly, the friction factor results are shown and discussed, followed by the heat transfer performance. Based on these results, new correlation approaches are proposed, adopting similar forms to those present in the literature, trying to capture the different trends exhibited by the present experimental data due to this new type of roughness.

4.2.1 Friction Factor

For each TO (AM1 and AM2), five pressure drop tests were carried out simultaneously with the heat transfer tests, as the Prandtl number is not expected to affect the friction factor. The experimental data are plotted in the Moody diagram in Figure 20.

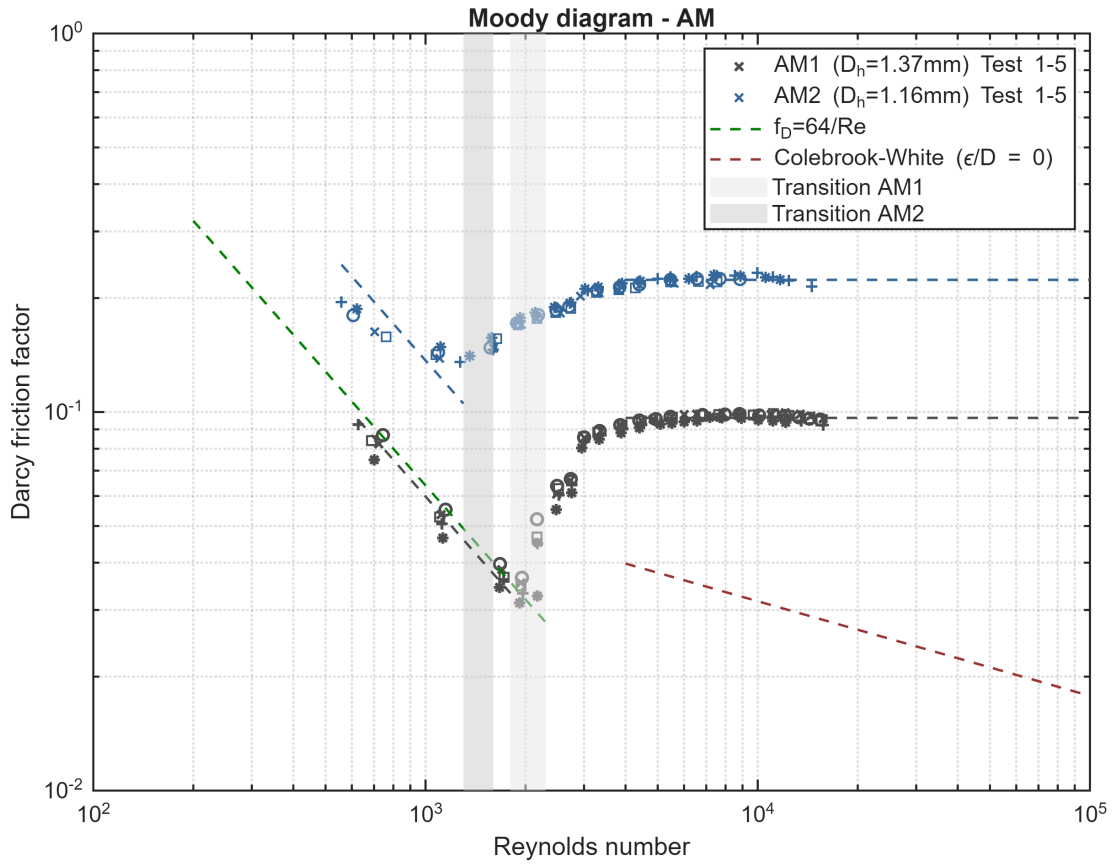

Figure 20: Friction factor for AM TOs on the Moody diagram

Table 9: Main flow results for AM1 and AM2 TOs in laminar and turbulent regimes

Test Object	D_h (mm)	$f_D \cdot Re$ (Laminar)	Re_{cr}	f_D (Turbulent)	ϵ/D_h
AM1	1.37	59.8	1300	0.097	0.09
AM2	1.16	136.9	1800	0.223	0.32

The experimental data of the Darcy friction factor in the turbulent regime, shown in Figure 20 and Table 9, indicate that both TOs exhibit a fully rough condition, since f_D is not a function of the Reynolds number but depends solely on the relative roughness. The relative roughness is governed by the hydraulic diameter, as the absolute roughness, determined by the alloy and the printing process, is the same for both TOs. Since only

limited information is available regarding the roughness, the equivalent relative roughness ϵ/D is extrapolated from the experimental data of f_D in the turbulent regime by inverting the Colebrook-White (Equation 33) for fully rough condition, as proposed by Stimpson [45].
In the laminar regime, the typical trend $f_D = A/Re$ is observed, with A being a function of the relative roughness, in agreement with the findings of Stimpson [45] and Huang [28]. For AM1, the constant A is lower than the theoretical laminar value for smooth channels (64), which is believed to be due to the high uncertainty of the experimental rig in this regime, as also highlighted in the Smooth validation. For AM2, it is unclear whether f_D depends strictly on $1/Re$ or whether an exponent on Re should be introduced to better capture the trend in the laminar regime. However, the limited number of data points, combined with the high uncertainty and the fact that only one TO exhibits this shift in the trend, prevents from drawing a definitive conclusion. The critical Reynolds number Re_{cr} at which the transition starts is lower compared to the Smooth condition ($Re_{cr} = 2300$) and depends on the roughness. Using the ϵ/D values previously computed from the Colebrook-White and including two other TOs results from the previous version of the rig [44], an interpolation between Re_{cr} and ϵ/D was performed. The resulting trend, visible in Figure 21, follows a hyperbolic reduction.

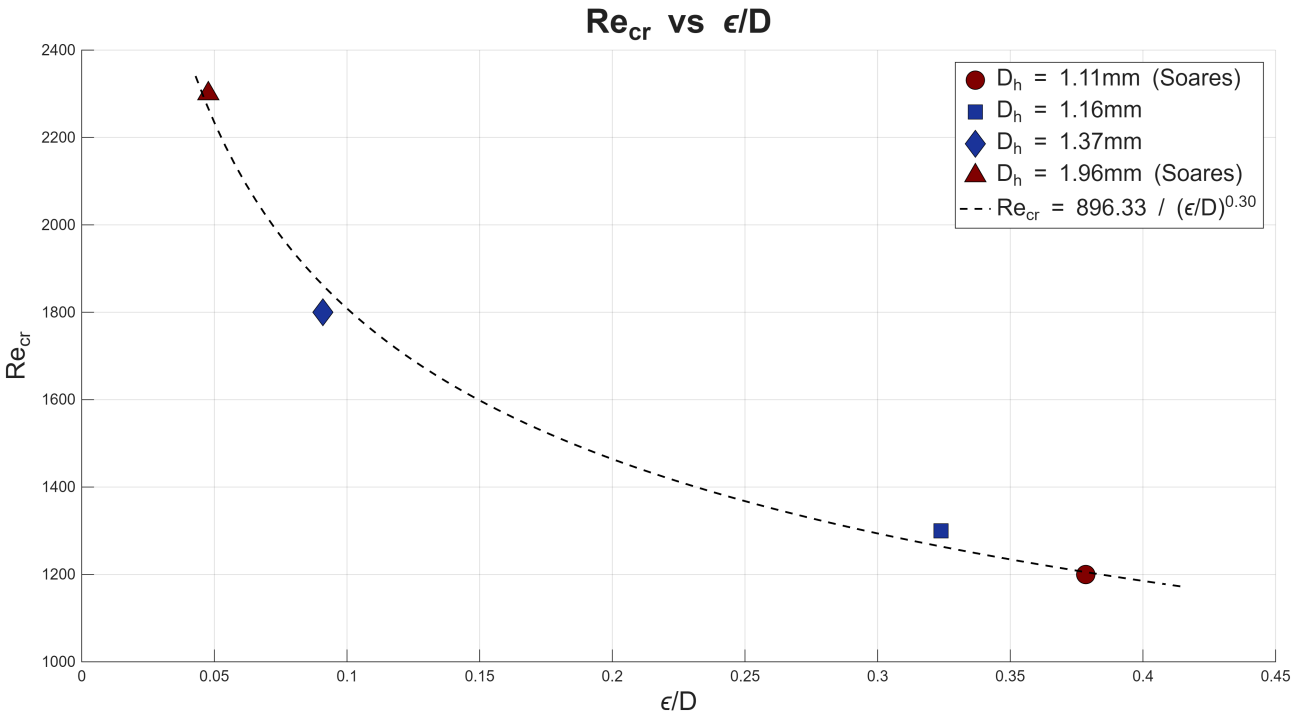

Figure 21: critical Reynolds for different hydraulic diameters

4.2.2 Heat Transfer

The same experimental campaign conducted for the pressure drop measurements was also used to evaluate the heat transfer performance. For each TO (AM1 and AM2), five different Prandtl numbers, ranging from 4 to 10.5, were tested. Due to the high uncertainty and instability in the laminar regime, only cases with $Re > 3000$ were analyzed. The results obtained for the turbulent regime are reported in Figure 22.

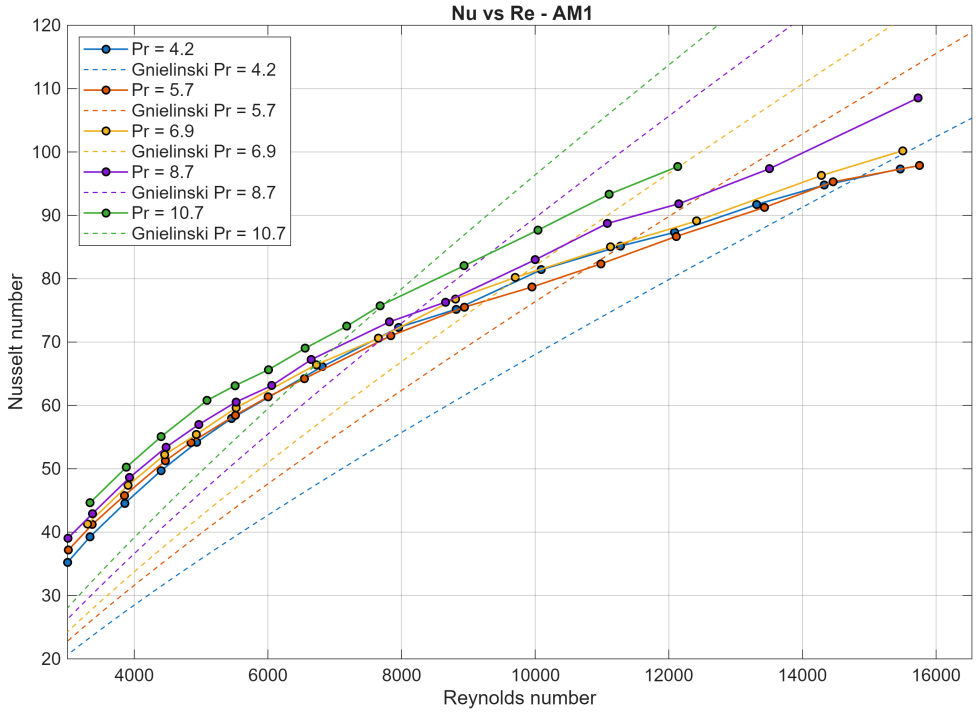

(a) AM1

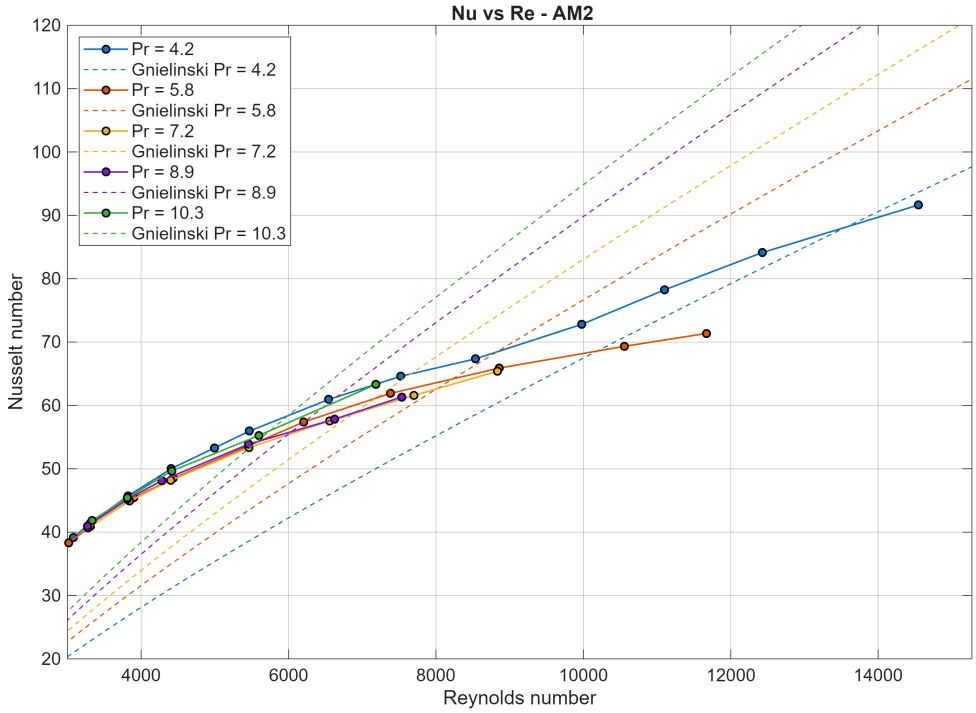

(b) AM2

Figure 22: Nu vs Re for AM TOs in turbulent regime

In Figure 22, the theoretical Gnielinski correlation for a smooth surface, corrected for the entry effect as described in Equation 54, is plotted for comparison and lies above the experimental data for all Prandtl numbers for aproximately $Re > 6000$. This behaviour is unexpected, since surface roughness is generally associated with an enhancement of heat transfer. The most plausible explanation lies in the nature of the roughness itself: the large roughness, combined with the low thermal conductivity of the INC939 alloy, generate a temperature gradient within the peaks, introducing an additional thermal resistance. This phenomenon is quantitatively evidenced by the Biot number, whose values reflect the presence of a significant conduction resistance inside the roughness peaks. Recalling the definition of Bi (Table 1), it can be rewritten as a function of the Nusselt number:

$$Bi = 2Nu \frac{R_z}{D_h} \frac{\lambda_f}{\lambda_s} \tag{60}$$

where $2R_z$ represents L_c for Biot number, since the roughness peaks are approximately hemispherical and the wetted surface is about twice the projected cross–sectional area. $R_z = 96.8$ μm was taken from pre-existing measurements in the laboratory for INC939 channels [44].
It should be noted that this approach approximates the local heat transfer coefficient around each asperity by the global average value. Although this assumption simplifies the calculation, it is expected to provide an adequate approximation of the physical behavior, as each asperity has a higher local h on the windward side and a lower local h on the leeward side relative to the global average. In Table 10 some values for Bi are reported as an example. These values exceed the commonly adopted threshold of $Bi < 0.1$ [29] for neglecting conduction effects within the solid, indicating that the roughness peaks actually act as an additional thermal resistance.

Table 10: Biot number for AM1 and AM2 at $Pr \approx 7$ for selected Reynolds numbers

Re	**Bi (AM1)**	**Bi (AM2)**
3000	0.286	0.335
5000	0.432	0.468
7000	0.515	0.541
9000	0.583	0.576

To account for the additional thermal resistance introduced by the roughness peaks, a correction to the experimental Nusselt number is proposed based on a simplified one-dimensional series resistance model. The corrected Nusselt number, representing the convective heat transfer coefficient without the conduction penalty, is approximated as:

$$Nu_{corr} = Nu(1 + Bi) \tag{61}$$

where Bi is computed for each experimental point with Equation 60. The corrected values for the Nusselt number are shown in Figure 23b. According to the experimental results of Stimpson [45], the trend is now much more reasonable, showing the effectiveness of the correction. Henceforth, all references to the Nusselt number will denote Nu_{corr}, isolating the convective contribution.

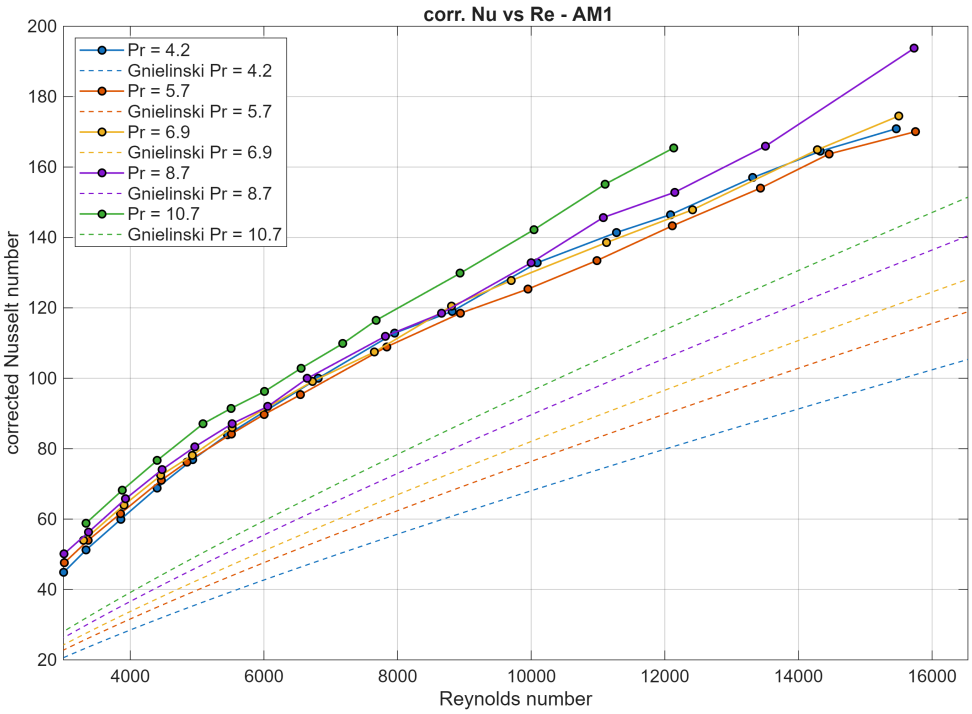

(a) AM1

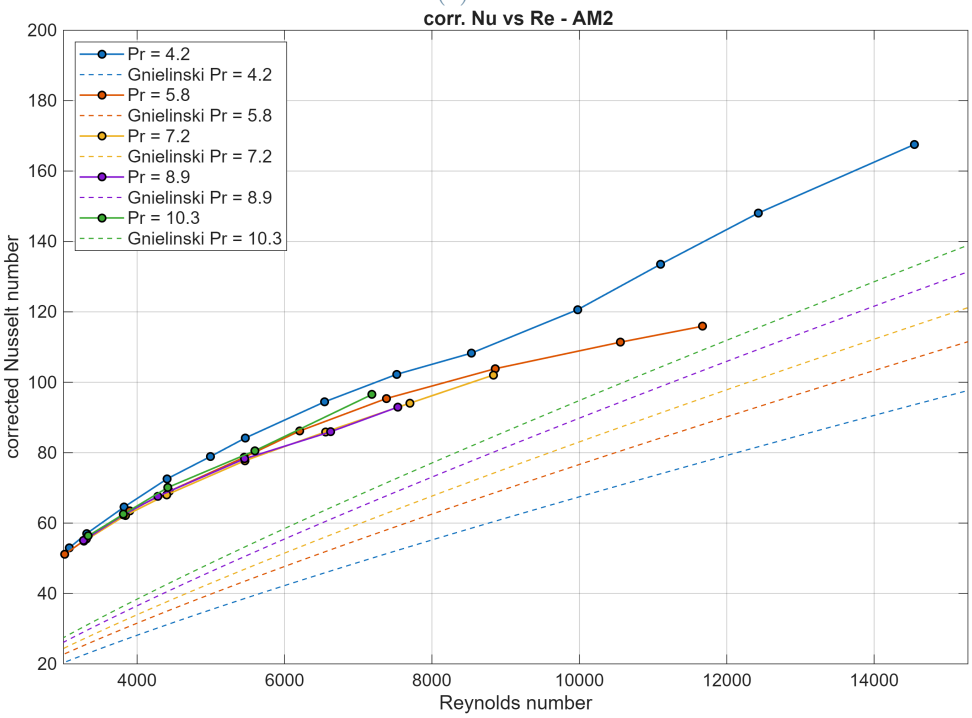

(b) AM2

Figure 23: Nu vs Re for AM TOs in turbulent regime, corrected for the Bi

In Figure 22 and 23, the Prandtl number appears to have a much smaller influence on heat transfer than in the smooth case, represented in the plots by the Gnielinski correlation. For AM2, the TO with the highest relative roughness, the Prandtl number seems even to have a negative effect, with the curve corresponding to the lower Pr showing a higher Nu. In Appendix A this effect is quantified through the fit $Nu_{corr} \sim Pr^m$ for selected Re values. For AM1 TO, m is positive but significantly lower than the theoretical prediction of 1/3. For AM2 TO, m is slightly negative; however, a complete inversion of the trend is not observed for each Pr. It must also be considered that all data at the same Re fall within a very narrow range, inside the uncertainty. This behaviour is consistent with the observations of Soares [44], who, under more extreme conditions (nominal

diameter of 1 mm), reported a complete inversion of the trend, with Pr having a strongly negative impact on heat transfer for that test object. AM1 and AM2 (nominal diameters of 1.5 mm and 1.25 mm, respectively) fall into an intermediate regime. Since all data lie very close to each other, within the calculated uncertainty range, a different approach has been adopted. The ratio between the experimental Nu (remembering it is corrected to isolate the convective contribution) and the Nu_0 for the smooth case (computed from the Gnielinski correlation under the same flow conditions, i.e., identical Re and Pr) is plotted against f_D/f_{Do}, where f_{D0} is obtained from the Colebrook–White equation, again for the smooth case. The resulting plot is shown in Figure 24.
The results show that the greatest enhancements occur for the lower Prandtl numbers. This appears to contradict the correlation proposed by Norris (Equation 1) for sand-grain roughness, which predicts greater enhancement at higher Pr. However, Norris [39] himself observed that, at high roughness levels, where the ceiling value of Nu/Nu_0 is reached (that is, where an increase in the friction factor no longer increases the Nu/Nu_0 ratio), Pr values above 4 (precisely the range investigated in this work) exhibit a slightly negative influence on Nu/Nu_0. This trend aligns well with the present findings, where the ceiling region is already exceeded for each test except for the lowest Pr for AM1, which still shows the typical plateau of the ceiling region for lower f_D/f_{D0}, while in all the other tests an increase in the friction factor ratio always corresponds to a decrease in heat transfer enhancement. Compared to Norris' data, the ceiling region in the present work, similarly to the results of Stimpson [45], is likely anticipated due to the anisotropic surface roughness induced by AM.
Extending Norris' findings to more extreme scenarios, such as those explored by Soares [44], it becomes plausible that a high Pr not only reduces the relative heat transfer augmentation due to roughness compared to a smooth surface, but may also directly decrease the Nusselt number as Pr increases, thereby providing further corroboration for the results reported by Soares and confirmed in this work.

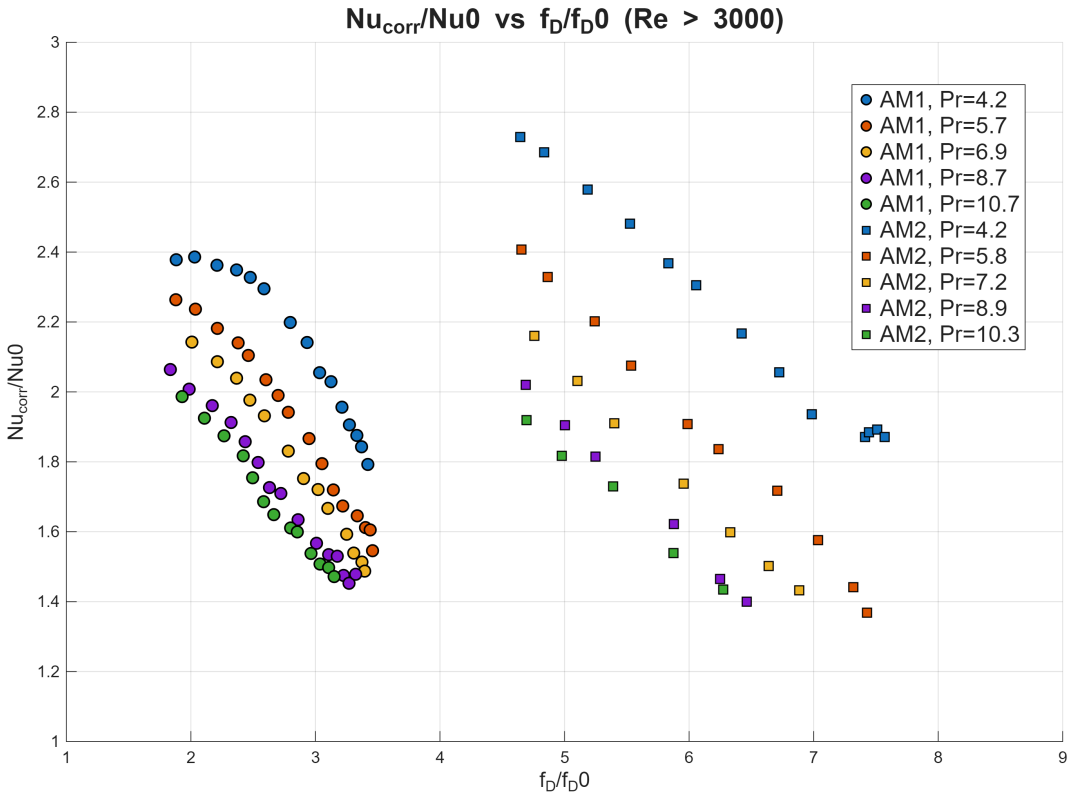

Figure 24: Nusselt augmentation vs friction factor augmentation

Starting from these considerations and applying the same form of the Norris correlation $Nu/Nu_0 = (f_D/f_{D0})^n$ to the present results, the following type of correlation is proposed for the exponent n:

$$n = K\,\mathrm{Re}^{a}\,\mathrm{Pr}^{\,b(\mathrm{f_D})} \tag{62}$$

with

$$b(\mathrm{f_D}) = b_0 - b_1\,\ln\left(\frac{\mathrm{f_D}}{\mathrm{f_{D0}}}\right) \tag{63}$$

This form must reflect the impact of Re in decreasing the heat transfer enhancement when increasing f_D/f_{D0}, while the effect of the Prandtl number depends on the roughness: for low roughness, the function $b(f_D)$ must

be positive, with Pr having a positive impact on the heat transfer enhancement, whereas for high roughness it must have a negative impact, as in the experimental data of this work. For very high roughness, as in the case of Soares, its impact must be so negative on the enhancement that it outweighs its positive impact in Nu_0, as it is in the Gnielinski, allowing the correlation to identify cases in which an increase in the Prandtl number results in a decrease in Nu, and therefore in heat transfer. Therefore, from a fit to the experimental data of this work, the following correlation for n, now expressed with the fitted coefficients, is obtained:

$$n = 73.9\,\mathrm{Re}^{-0.455}\,\mathrm{Pr}^{0.0829-0.4952\,\ln\left(\frac{f_D}{f_{D0}}\right)} \tag{64}$$

With n, it is then possible to compute the predicted Nusselt number, as Nu_0 and f_{D0} come from well-known correlations and f_D is an experimental input.
A parity plot comparing the proposed correlation predictions with the experimental data is presented in Figure 25.

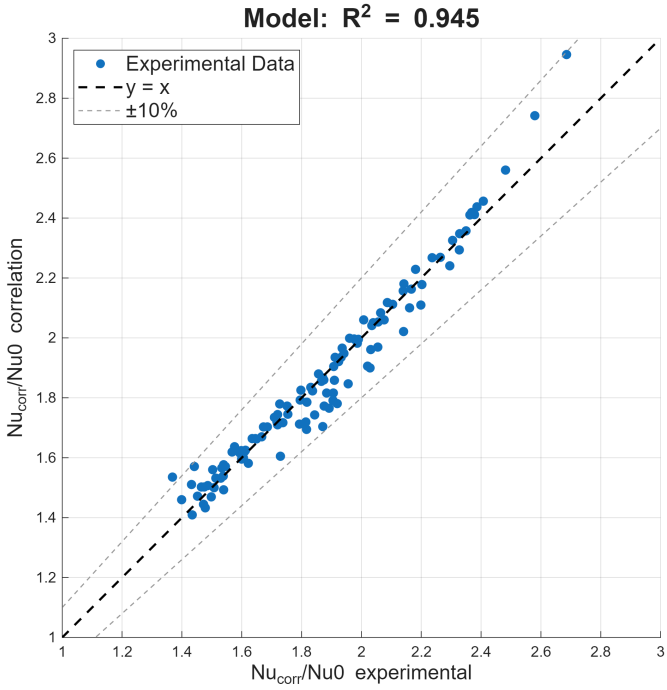

Figure 25: parity plot of the proposed correlation against all experimental data

4.3. Discussion of the Results

The results obtained for the Smooth TO fully validate the experimental rig and procedure in the turbulent regime, both in terms of pressure drop and heat transfer. The rig is able to reliably reproduce well-known correlations for a smooth tube in turbulent regime, such as those of Colebrook-White and Gnielinski. In the laminar regime, however, the rig does not yet sufficiently reproduce the theoretical expression for friction factor. This limitation is mainly due to the large measurement range (and thus higher uncertainty) of the differential pressure transmitters. Regarding heat transfer, only a few data points were collected in the laminar regime, but their comparison with known solutions, corrected for entrance effects, appears promising.
For the additively manufactured test objects (AM1 and AM2), the pressure drop analysis highlights the following:

- **Turbulent regime:** A fully rough condition is observed, with the friction factor depending solely on the relative roughness and not on the Reynolds number. In the absence of a clear roughness parameter, it is suggested to invert the usual use of the Colebrook-White equation, estimating the equivalent relative roughness from the measured friction factor.
- **Laminar regime:** Higher relative roughness increases the friction factor even in laminar flow. However, it is still unclear whether the $f_D \propto Re^{-1}$ trend persists at very high roughness, or if $f_D \propto Re^{-n}$ with $n \neq 1$ would better capture the behaviour.

– **Transition regime:** The critical Reynolds number at which transition begins depends on the relative roughness, occurring earlier for higher roughness values. An interpolation (hyperbolic fit) linking the critical Reynolds number to the equivalent relative roughness is proposed. Further tests with channels of different hydraulic diameters are needed to fully characterize this effect.

These observations are consistent with the theory [50] and the experimental findings on AM-printed channels [9, 45] and rough minichannels [28].
The heat transfer campaign was evaluated only in the turbulent regime due to instability issues in the laminar regime. The experimental data exhibits an unexpected drop at the higher tested Reynolds numbers ($Re > 6000/7000$), with the Gnielinski correlation for smooth tubes, under the same flow conditions, predicting higher values than those measured for the rough case, which is not expected since the roughness should enhance the heat transfer. This behavior is attributed to the low thermal conductivity of INC939 combined with the high surface roughness, which together result in a Biot number greater than 0.1, introducing an undesired effect due to solid conduction resistance. To isolate the convective effects from the conductive resistance, the raw experimental results were corrected by multiplying them by $(1 + Bi)$. This correction method may introduce various approximations, and for future work, it is recommended to test alloys with higher thermal conductivity, but keeping in mind that this issue could arise again for higher Reynolds numbers. The correction was considered valid, and further considerations were made on the corrected data, since the trend with the correction is very similar to that of Stimpson [45] testing AM channels with air.
For both raw and corrected data, the effect of the Prandtl number on the Nusselt number does not appear to match that predicted by typical correlations. It is not believed to be an effect related to the Biot, as both datasets, raw and corrected, show the same unusual behavior. This phenomenon is not entirely new: the previous version of the rig, under extreme conditions, appeared to exhibit a complete inversion of the classical Pr–Nu trend [44]. This is partially supported by previous works on sand–grain rough channels [39], which reported that, for high roughness levels, the Prandtl number tends to attenuate the heat transfer enhancement due to roughness compared to the smooth case. The proposed empirical relation, linking the ratio between the experimental (and corrected) Nu over Nu_0 from Gnielinski and the ratio between the experimental f_D and f_{D0} from the Colebrook for smooth condition with an exponent n, as $\frac{Nu}{Nu_0} = \left(\frac{f_D}{f_{D0}}\right)^n$, is inspired by the correlation proposed by Norris (Equation 1), aiming to determine the value of n, but differs because n is also dependent on Reynolds number and friction factor, not solely on Prandtl number as in Norris' case. The form of the correlation for n accounts for the possibility that roughness may invert the effect of Prandtl number both on the enhancement of heat transfer relative to the smooth case, as observed for the TOs tested in this work, and even cause Prandtl number to have a negative effect on heat transfer in general, as in the extreme case of AM2 TO and the one tested by Soares [44]. The fit (Equation 62), although being good, with $R^2 = 0.945$ and thus supporting the physical sense of the proposed form, was performed using only the experimental data of the two TOs from this work. For this reason, it is believed that future work, testing more TOs with different hydraulic diameters, will slightly change the coefficients of the correlation. While the empirical correlation attempts to capture the variation of the Prandtl effect on heat transfer with changing roughness, no physical explanation is currently available and the cause of this effect remains unknown.

5. Conclusion and Future Work

5.1. Conclusion

The redesigned hydraulic circuit delivered precise and reliable results for both flow and heat transfer performance in the turbulent regime, as confirmed by the validation tests. Minor refinements are required, such as the integration of more accurate measurement instruments (especially for the differential pressure transmitter and the Coriolis mass-flow meter), if the laminar regime becomes a focus of future investigations.
The uncertainty analysis showed acceptable results; however, for the heat transfer case, a broader application of the Monte Carlo method to all input parameters is recommended. Since the effect under investigation is new, a highly accurate uncertainty quantification is essential to ensure that the observed trend is genuine and not an artifact of measurement errors.
For the additively manufactured test objects, the experimental friction factor data confirmed the trends reported in previous studies [9] [45] [28], showing an increase in the friction factor with relative roughness in both laminar and turbulent regimes. In the turbulent regime, a fully rough condition was reached, from which the equivalent roughness was determined. As expected, increasing relative roughness was observed to shift the transition threshold to lower Reynolds numbers, and a hyperbolic fit was derived (Figure 21) linking the critical Reynolds number to the equivalent roughness. Considering the constraints of the experimental set-up, the high viscosity of water leads to significant pressure drop (8–10 bar) at Reynolds numbers of a few tens of thousands. Therefore,

analyses in the turbulent regime could be more easily conducted using air as the working fluid, while in the laminar regime water offers the advantage of producing sufficiently large pressure drop to be captured without the need for extremely precise instruments.
The core of this work concerns the effect of the Prandtl number on heat transfer. The analysis revealed that high surface roughness levels, combined with the low thermal conductivity of INC939, resulted in an additional conduction resistance that interfered with the desired convective measurements. This effect was effectively isolated and accounted for, but should be avoided in future experiments whenever possible. The influence of the Prandtl number on heat transfer enhancement was then examined, and a correlation (Equation 62) was proposed to capture its varying impact with respect to surface roughness. This behavior appears to be poorly documented in the literature. It has been observed in the present study and in tests performed with the previous version of the rig [44], but it has only limited corroborations from other works, such as that of Norris [39]. Since the effect is new and a physical explanation is still lacking, further experimental investigations are required to confirm its validity and generally to better understand the phenomenon.

5.2. Future Work

The following suggestions are proposed to continue this research:

1. It is strongly suggested to test only channels printed using highly thermal conductive alloys, in order to absolutely avoid $Bi > 0.1$ and prevent the need to account for the conductive resistance caused by the roughness a posteriori.
2. To attach the Pt100 on the external surface of the test object instead of using aluminum tape, a two-part epoxy was ordered to ensure better contact between the test object and the temperature measurements. Although it did not arrive in time for this work, it is suggested to try this solution for the future tests.
3. If in the future the laminar regime is desired to be investigated, only simple changes to the rig would be required, such as replacing both the differential pressure transmitter and the Coriolis mass flow meter with more precise instruments.
4. A more detailed uncertainty analysis should be conducted using the Monte Carlo method, applied to each input across several Reynolds and Prandtl numbers and for different hydraulic diameters. This is necessary to ensure that no physical effects are mistakenly attributed to uncertainty and that the results can be interpreted with confidence.
5. To better capture the effect of the Prandtl number on heat transfer, more extreme conditions should be tested, such as using test objects with very small hydraulic diameters (e.g., 0.75 mm or 1 mm).
6. Since small diameters significantly increase the relative roughness, the pressure drop can easily reach values above 20 bar, even at low Reynolds numbers. This was already a strong limitation of the rig for the tested TOs. The rig, specifically the test section and the hydraulic circuit, could be modified to withstand higher pressures than the current limit of 15 bar.
   An alternative and interesting approach may be to replace water with different fluids, such as hydrofluoroethers (HFE) and perfluorocarbons (PFC) [55]. These fluids are safe (non-toxic, non-flammable, chemically inert, and non-corrosive), easy to handle, and have a significantly lower dynamic viscosity compared to water, while maintaining a Prandtl number that varies with temperature within the same range as that of water. They are dielectric fluids, allowing the Joule heating effect to be used in the rig. The reduction in viscosity would lower the pressure drop for a given friction factor, enabling tests at higher Reynolds numbers and higher relative roughness.
7. It would be very interesting to test the flow and heat transfer performance not only in single-phase conditions, but also in two-phase, both with water or, more easily, with the proposed fluids [34], which have lower boiling temperatures. The high and anisotropic roughness could strongly enhance flow boiling, and therefore the heat transfer coefficient. This would require a complete redesign of the rig, but could lead to very promising results.

Some of these suggestions may be easier to implement than others, while a few would require significant modifications or even the complete rethinking of the experimental setup. Nonetheless, it is believed that they all represent valuable directions for the continuation of this research.

List of Acronyms

Acronym	Description
AB	Aktiebolag
AC	Alternating Current
AM	Additive Manufacturing
AM1	First Additive Manufactured Test Object
AM2	Second Additive Manufactured Test Object
CAD	Computer-Aided Design
CFD	Computational Fluid Dynamics
CoCr	Cobalt-Chromium (alloy)
CO_2	Carbon Dioxide
CSP	Concentrated Solar Power
DMLS	Direct Metal Laser Sintering
HFE	Hydrofluoroethers
LES	Large Eddy Simulation
LPBF	Laser Powder Bed Fusion
MAPE	Mean Absolute Percentage Error
PDF	Probability Density Function
PFC	Perfluorocarbons
PID	Proportional-Integral-Derivative (control)
PIV	Particle Image Velocimetry
Pt100	Platinum Resistance Thermometer (100 ohms at 0°C)
R&D	Research and Development
RS	RS Components (Swedish industrial components distributor)
RSS	Root Sum Square
SEM	Standard Error of the Mean
TO	Test Object

List of Symbols

Symbol	Description	Unit
	Latin symbols	
A_c	Cross-sectional area	m^2
Bi	Biot number	–
C_f	Fanning friction factor	–
c_p	Specific heat at constant pressure	J/(kg·K)
D_h	Hydraulic diameter	m
f_D	Darcy friction factor	–
g	Gravitational acceleration	m/s^2
h	Average heat transfer coefficient	$W/(m^2·K)$
k	Coverage factor for confidence intervals	–
k_s	Nikuradse equivalent sand-grain roughness	μm
L_c	Characteristic length	m
L_e	Entrance length	m
$\dot{m}$	Mass flow rate	kg/s
Nu	Nusselt number	–
P	Wetted perimeter	m
p	Pressure	Pa
Pe	Peclet number	–
Pr	Prandtl number	–
$\dot{Q}$	Heat transfer rate	W

Symbol	Description	Unit
q_s''	Surface heat flux	$\mathrm{W/m^2}$
R^2	Coefficient of determination	–
Re	Reynolds number	–
R_z	Mean roughness depth	μm
St	Stanton number	–
T	Temperature	K
u	Bulk velocity	m/s
$\mathbf{v}$	Velocity vector	m/s
X_i	Direct measurement	(depends)
	Greek symbols	
α	Thermal diffusivity	$\mathrm{m^2/s}$
Δ	Microscope resolution	μm
ΔT	Temperature difference	K
δ	Boundary layer thickness	m
δ_t	Thermal boundary layer thickness	m
δX_i	Total uncertainty of direct measurement	(depends)
ε	Equivalent roughness	μm
λ	Thermal conductivity	W/(m·K)
μ	Dynamic viscosity	Pa·s
ν	Kinematic viscosity	$\mathrm{m^2/s}$
ρ	Fluid density	$\mathrm{kg/m^3}$
σ	Standard deviation	(depends)
τ_w	Wall shear stress	Pa
θ	Non-dimensional temperature	–
Φ	Viscous dissipation function	$\mathrm{s^{-2}}$
	Subscripts	
0	Reference	
b	Bulk	
calc	Computed from simulation	
corr	Corrected	
cr	Critical (Re)	
ext	External wall of test object	
f	Fluid	
in	Inlet of test object	
int	Internal wall of test object	
loc	Local	
m	Mean between inlet and outlet	
out	Outlet of test object	
s	Solid	
w	Wall	
water	Water	
x	At position x	
∞	Freestream	

References

[1] Adrian Bejan. *Convection Heat Transfer*. Wiley, Hoboken, NJ, 4 edition, 2013.

[2] Ian H. Bell, Jorrit Wronski, Sylvain Quoilin, and Vincent Lemort. Pure and pseudo-pure fluid thermophysical property evaluation and the open-source thermophysical property library coolprop. *Industrial & Engineering Chemistry Research*, 53(6):2498–2508, February 2014.

[3] H. Breuer. Better turbines thanks to 3d printing. `https://www.siemens-energy.com/global/en/home/stories/better-turbines-thanks-to-3d-printing.html`, 2018. Accessed: Aug. 14, 2025.

[4] Aaron Brugnera. Experimental investigation of heat transfer in additive manufactured channels with different prandtl numbers. Master's thesis, Politecnico di Torino, Torino, Italy, October 2024.

[5] F. Calignano, D. Manfredi, E. P. Ambrosio, L. Iuliano, and P. Fino. Influence of process parameters on sur-

face roughness of aluminum parts produced by dmls. *The International Journal of Advanced Manufacturing Technology*, 67(9), December 2012.

[6] Francesco Careri, Raja H.U. Khan, Catherine Todd, and Moataz M. Attallah. Additive manufacturing of heat exchangers in aerospace applications: a review. *Applied Thermal Engineering*, 235, November 2023.

[7] Lokesh Chandrabalan, Markus Baier, Roberto Meloni, Marco Pieri, Luca Ammannato, Eugenio Del Puglia, and Simone Carmignato. Non-destructive assessment of the functional diameter and hydrodynamic roughness of additively manufactured channels. *Applied Sciences*, 13(10), May 2023.

[8] Stuart W. Churchill. Comprehensive correlating equations for heat, mass and momentum transfer in fully developed flow in smooth tubes. *Industrial and Engineering Chemistry Fundamentals*, 16(1):109–116, 1977.

[9] Ivel L. Collins, Justin A. Weibel, Liang Pan, and Suresh V. Garimella. Evaluation of additively manufactured microchannel heat sinks. *IEEE Transactions on Components, Packaging and Manufacturing Technology*, 9(3), March 2019.

[10] M. G. Cooper, B. B. Mikic, and M. M. Yovanovich. Thermal contact conductance. *International Journal of Heat and Mass Transfer*, 12(3), March 1969.

[11] Corson L. Cramer, Edgar Lara-Curzio, Amy M. Elliott, Trevor G. Aguirre, Bola Yoon, Brian A. Fricke, Vivek Rao, Prashant Jain, and Kashif Nawaz. Material selection and manufacturing for high-temperature heat exchangers: Review of state-of-the-art development, opportunities, and challenges. *International Journal of Ceramic Engineering & Science*, 6(5), July 2024.

[12] Jordi Delgado, Joaquim Ciurana, and Ciro A. Rodríguez. Influence of process parameters on part quality and mechanical properties for dmls and slm with iron-based materials. *The International Journal of Advanced Manufacturing Technology*, 60(5-8), September 2011.

[13] Divyansh Singh Dev, Avala Raji Reddy, and Mahender Thotakuri. Powder bed fusion process: A brief review. *Materials Today Proceedings*, September 2020. Figure 6: DMLS Setup.

[14] D. F. Dipprey and R. H. Sabersky. Heat and momentum transfer in smooth and rough tubes at various prandtl numbers. *International Journal of Heat and Mass Transfer*, 6(5):329–353, 1963.

[15] Wenchao Du, Wenhua Yu, David M. France, Mrityunjay Singh, and Dileep Singh. Additive manufacturing and testing of a ceramic heat exchanger for high-temperature and high-pressure applications for concentrating solar power. *Solar Energy*, 236, April 2022.

[16] Siemens Energy. About siemens energy. `https://www.siemens-energy.com/global/en/home/company/about.html`, 2025. Accessed: Aug. 14, 2025.

[17] Siemens Energy. Siemens energy in sweden. `https://www.siemens-energy.com/se/en/home.html`, 2025. Accessed: Aug. 14, 2025.

[18] A. Frankel. Digitalization enables industrialization of additive manufacturing. `https://blogs.sw.siemens.com/thought-leadership/digitalization-enables-industrialization-of-additive-manufacturing/`, 2025. Accessed: Aug. 14, 2025.

[19] Himani Garg, Guillaume Sahut, Erika Tuneskog, Karl-Johan Nogenmyr, and Christer Fureby. Large eddy simulations of flow over additively manufactured surfaces: Impact of roughness and skewness on turbulent heat transfer. *Physics of Fluids*, 36(8), August 2024.

[20] Himani Garg, Lei Wang, and Christer Fureby. Heat transfer enhancement with additively manufactured rough surfaces: Insights from large-eddy simulations. *Physics of Fluids*, 36(2), February 2024.

[21] Payam Shams Ghahfarokhi, Ants Kallaste, Anouar Belahcen, and Toomas Vaimann. Analytical thermal model and flow network analysis suitable for open self-ventilated machines. *IET Electric Power Applications*, 14(6):929–936, 2020. Figure 5: Boundary-layer development inside the cooling ducts.

[22] Afshin J. Ghajar and Lap-Mou Tam. Heat transfer measurements and correlations in the transition region for a circular tube with three different inlet configurations. *Experimental Thermal and Fluid Science*, 8(1):79–90, 1994.

[23] Ian Gibson, David W. Rosen, and Brent Stucker. *Powder Fusion Mechanism*, chapter 5.3, pages 130–131. Springer, Berlin, Germany, 3 edition, 2021.

[24] Fabio Gissi. Infrared thermography-based heat transfer analysis and thermal boundary layer evaluation on upscaled models of additively manufactured rough surfaces. Master's thesis, Politecnico di Torino, Torino, Italy, July 2025.

[25] V. Gnielinski. Heat transfer in laminar flow. *VDI Heat Atlas*, 2, 2010.

[26] V. Gnielinski. On heat transfer in tubes. *International Journal of Heat and Mass Transfer*, 63:134–140, 2013.

[27] Ragnar Holm and Else Holm. *Electric Contacts: Theory and Application*. Springer-Verlag, Berlin, Heidelberg, 4 edition, 1967.

[28] K. Huang, J. W. Wan, C. X. Chen, Y. Q. Li, D. F. Mao, and M. Y. Zhang. Experimental investigation on friction factor in pipes with large roughness. *Experimental Thermal and Fluid Science*, 50(10):147–153, October 2013.

[29] Frank P. Incropera, David P. DeWitt, Theodore L. Bergman, and Adrienne S. Lavine. *Fundamentals of Heat and Mass Transfer*. John Wiley & Sons, Hoboken, NJ, 6 edition, 2007.

[30] Mohammadreza Kadivar, David Tormey, and Gerard McGranaghan. A review on turbulent flow over rough surfaces: Fundamentals and theories. *International Journal of Thermofluids*, 10:100077, 2021.

[31] Kathryn L. Kirsch and Karen A. Thole. Heat transfer and pressure loss measurements in additively manufactured wavy microchannels. *Journal of Turbomachinery*, 139(1), September 2016.

[32] Daeyoung Kong, Euibeen Jung, Kyupaeck Jeff Rah, Yunseo Kim, Han Sang Kim, Vivek Vardhan Manepalli, Yongtaek Hong, Hyoung Gil Choi, Hyoungsoon Lee, and Damena Agonafer. An additively manufactured manifold-microchannel heat sink for high-heat flux cooling. *International Journal of Mechanical Sciences*, 248, June 2023.

[33] Modesto Laguardia. Impact of am-induced upscaled surface roughness on flow dynamics, heat transfer and friction properties: A particle image velocimetry study. Master's thesis, Politecnico di Torino, Torino, Italy, July 2025.

[34] K.C. Leong, J.Y. Ho, and K.K. Wong. A critical review of pool and flow boiling heat transfer of dielectric fluids on enhanced surfaces. *Applied Thermal Engineering*, 112, February 2017.

[35] Yan Li, Qing Su, Guojun Sheng, Seyed Reza Elmi Hosseini, Bassam Edmond Badran, Ping Gong, Chenxing Xin, and Huasheng Wang. Recent advances in artificial-intelligence enhanced additive manufacturing of heat exchangers for thermal management: a review. *Materials & Design*, 256, October 2025.

[36] Robert J. Moffat. Describing the uncertainties in experimental results. *Experimental Thermal and Fluid Science*, 1(1):3–17, 1988.

[37] Seyed A. Niknam, Mehdi Mortazavi, and Dongsheng Li. Additively manufactured heat exchangers: a review on opportunities and challenges. *The International Journal of Advanced Manufacturing Technology*, 112(3), January 2021.

[38] J. Nikuradse. Laws of flow in rough pipes. Technical Memorandum 1292, National Advisory Committee for Aeronautics, November 1950. Translation of "Strömungsgesetze in rauhen Rohren," VDI-Forschungsheft 361, Beilage zu "Forschung auf dem Gebiete des Ingenieurwesens," Ausgabe B, Band 4, July/August 1933.

[39] R. H. Norris. Some simple approximate heat transfer correlations for turbulent flow in ducts with surface roughness. *Augmentation of Convection Heat and Mass Transfer*, 1971.

[40] Syed Abbas Raza, Olcay Ersel Canyurt, and Hüseyin Kürşad Sezer. A systematic review of inconel 939 alloy parts development via additive manufacturing process. *Heliyon*, 10(3), February 2024.

[41] Warren M. Rohsenow, James P. Hartnett, and Young I. Cho, editors. *Handbook of Heat Transfer*. McGraw-Hill, New York, NY, 3 edition, 1998.

[42] Ramon Peruchi Pacheco da Silva, Kashif Nawaz, Hyun Jin Kim, M. Muneeshwaran, Easwaran N. Krishnan, and Xiangyu Li. Advances in high-pressure and high-temperature heat exchangers: Innovations via additive manufacturing and their applications. *Thermal Science and Engineering Progress*, 65, September 2025.

[43] Jacob C. Snyder and Karen A. Thole. Effect of additive manufacturing process parameters on turbine cooling. *Journal of Turbomachinery*, 142(5), April 2020.

[44] Isa Eduarda Baptista Soares. Experimental investigation on forced convective heat transfer and pressure loss for additively manufactured cooling channels. Master's thesis, Universidade do Porto, Faculty of Engineering, Porto, Portugal, September 2024. Available at: https://hdl.handle.net/10216/162216.

[45] Curtis Stimpson, Karen A. Thole, Jacob Snyder, and David J. Mongillo. Roughness effects on flow and heat transfer for additively manufactured channels. *Journal of Turbomachinery*, 138(5), December 2015.

[46] Curtis K. Stimpson, Jacob C. Snyder, Karen A. Thole, and Dominic Mongillo. Scaling roughness effects on pressure loss and heat transfer of additively manufactured channels. *Journal of Turbomachinery*, 139(2), February 2017.

[47] Chunhua Sun and Guangqing Shang. Application of technology of additive manufacturing in radiators and heat exchangers. *Journal of Power and Energy Engineering*, 10, November 2022.

[48] Sicheng Sun, Tiago Augusto Moreira, Behzad Rankouhi, Xinyi Yu, Ian W. Jentz, Dan J. Thoma, Mark H. Anderson, and Xiaoping Qian. Topology optimization, additive manufacturing and thermohydraulic testing of high-temperature heat exchangers. *International Journal of Heat and Mass Transfer*, 242, June 2025.

[49] Dawid Taler. A new heat transfer correlation for transition and turbulent fluid flow in tubes. *International Journal of Thermal Sciences*, 108:108–122, 2016.

[50] Frank M. White. *Fluid Mechanics*. McGraw-Hill, New York, NY, 5 edition, 2002.

[51] Wikimedia Commons. Moody Diagram. `https://commons.wikimedia.org/wiki/File:Moody_EN.svg`, 2007. Licenza CC BY-SA 3.0.

[52] Alexander J. Wildgoose and Karen A. Thole. Heat transfer and pressure loss of additively manufactured internal cooling channels with various shapes. *Journal of Turbomachinery*, 145(7), February 2023.

[53] Liming Yao, Aditya Ramesh, Zhongmin Xiao, Yang Chen, and Quihui Zhuang. Multimetal research in powder bed fusion: A review. *Materials*, 16(12), 2023.

[54] Omar M. Zaki, Stefan Elbel, Robert A. Stavins, Nenad Miljkovic, Mario Wenzel, Andrew Musser, and William P. King. Additively manufactured compact water-cooled refrigerant condenser. *International Journal of Heat and Mass Transfer*, 244, July 2025.

[55] Shuai Zheng, Chuansheng Su, Xiaoping Yang, Yuantong Zhang, Kaiwen Duan, Yuan Zhang, Zhandong Huang, Yonghai Zhang, Fan Liu, and Jinjia Wei. A comprehensive review of single-phase immersion cooling in data centres. *Applied Thermal Engineering*, 272, August 2025.

A. Appendix A

Table 12: Fit $Nu_{corr} \sim \mathrm{Pr}^m$ for AM1 TO

Re (±5%)	**Re**	**Pr**	**Nu**	**m**
3300	3339	4.2	51.25	0.14
	3372	5.7	54.01	
	3302	6.9	53.93	
	3374	8.7	56.27	
	3336	10.7	58.81	
3900	3858	4.2	59.93	0.14
	3853	5.7	61.57	
	3907	6.9	63.99	
	3931	8.7	65.76	
	3880	10.7	68.20	
4400	4401	4.2	68.85	0.11
	4464	5.7	71.04	
	4456	6.9	72.40	
	4475	8.7	74.06	
	4402	10.7	76.64	
5000	4935	4.2	76.91	0.13
	4848	5.7	76.22	
	4929	6.9	78.15	
	4967	8.7	80.54	
	5090	10.7	87.09	
5500	5456	4.2	84.00	0.09
	5513	5.7	84.19	
	5526	6.9	85.96	
	5523	8.7	87.09	
	5506	10.7	91.43	
8800	8818	4.2	119.02	0.07
	8938	5.7	118.46	
	8806	6.9	120.46	
	8658	8.7	118.44	
	8938	10.7	129.85	
10000	10092	4.2	132.84	0.08
	9954	5.7	125.36	
	9701	6.9	127.77	
	10001	8.7	132.84	
	10043	10.7	142.22	
11100	11278	4.2	141.42	0.11
	10983	5.7	133.44	
	11128	6.9	138.56	
	11078	8.7	145.67	
	11108	10.7	155.16	
12200	12084	4.2	146.47	0.13
	12109	5.7	143.28	
	12415	6.9	147.87	
	12149	8.7	152.85	
	12133	10.7	165.45	

Table 13: Fit $Nu_{corr} \sim \mathrm{Pr}^m$ for AM2 TO

Re (±5%)	**Re**	**Pr**	**Nu**	**m**
3300	3314	4.2	57.00	-0.02
	3313	5.8	55.52	
	3279	7.2	54.84	
	3272	8.9	55.04	
	3335	10.3	56.36	
3800	3824	4.2	64.58	-0.04
	3898	5.8	63.48	
	3840	7.2	62.17	
	3814	8.9	62.33	
	3813	10.3	62.52	
4400	4408	4.2	72.58	-0.05
	4438	5.8	69.05	
	4400	7.2	68.03	
	4281	8.9	67.61	
	4416	10.3	70.11	
5500	5469	4.2	84.19	-0.05
	5452	5.8	78.68	
	5461	7.2	77.71	
	5457	8.9	78.26	
	5600	10.3	80.57	
7400	7524	4.2	102.27	-0.07
	7382	5.8	95.39	
	7700	7.2	94.06	
	7535	8.9	92.93	
	7187	10.3	96.53	
8700	8536	4.2	108.28	-0.11
	8860	5.8	103.86	
	8836	7.2	102.07	

Abstract in lingua italiana

Questa tesi si concentra sullo studio di canali di raffreddamento realizzati mediante Additive Manufacturing (AM). Tale tecnologia offre un elevato grado di libertà progettuale, permettendo l'ottimizzazione di scambiatori di calore e componenti di turbomacchine impossibili da realizzare con tecniche convenzionali. La rugosità superficiale anisotropa, causata dal processo di stampa, influenza però in modo significativo la dinamica del flusso e le prestazioni termiche, rendendo quindi necessario lo sviluppo di specifiche correlazioni. L'obiettivo di questo lavoro è indagare sperimentalmente l'influenza del numero di Prandtl sul trasferimento di calore, utilizzando come fluido di raffreddamento l'acqua, in canali realizzati utilizzando la tecnica di additive manufacturing per metalli più diffusa, la Laser Powder Bed Fusion (LPBF). Sono state condotte prove su un canale di riferimento liscio, a scopo di validazione, e su due provini realizzati in additive manufacturing , con diversi diametri idraulici. I risultati confermano che il banco prova è in grado di riprodurre le correlazioni classiche per il regime turbolento nel provino liscio, sia per quanto riguarda la perdita di carico che per il trasferimento di calore. Le analisi sui canali di raffreddamento stampati in AM mostrano che un aumento del numero di Prandtl non porta sempre a un incremento del trasferimento di calore, in contrasto con la teoria classica. Per descrivere questo effetto è stata proposta una nuova correlazione basata sui dati sperimentali dei due canali di raffreddamento testati. Questo lavoro rappresenta solo un primo passo nella comprensione di questo nuovo fenomeno e ulteriori indagini sono necessarie.

Parole chiave: trasferimento di calore; additive manufacturing; numero di prandtl; rugosità superficiale; canali di raffreddamento

Acknowledgements

To my family, for their unconditional love and support. A cherished memory of my grandfather, Ernesto, who has always been, and remains, a role model in my life. His values continue to guide me every day.
My deepest gratitude to my advisor, Prof. Andrea Lucchini, for his patience and constant availability, and to my supervisor Mats Kinell and to Alessio Bonaldo for the trust placed in me.
A special thanks to all my friends at Siemens Energy in Finspång, friends first and colleagues second, who helped me grow both professionally and personally. In particular, to Isa for her crucial support at the beginning of the project, to Fabio and Modesto for having shared this journey with me, and to Felipe for the conversations during our breaks about doubts, difficulties, and the progress of our respective research — but more often about life or football.
A thought for the Ukrainian people, unjustly afflicted by the war and forced to live every day with its consequences. Their courage and resilience are for me a source of inspiration and hope.